J. Fluid Mech. (2025), *vol.* 1017, A30, doi:10.1017/jfm.2025.10479

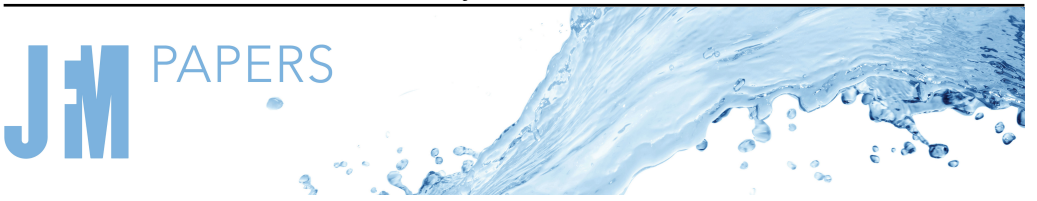

Turbulence–chemistry interaction in a non-equilibrium hypersonic boundary layer

Christopher Thomas Williams[1], **Mario Di Renzo**[1,2] **and Parviz Moin**[1]

[1]Center for Turbulence Research, Stanford University, Stanford, CA 94305, USA

[2]Department of Engineering for Innovation, Universitá del Salento, Lecce, Italy

Corresponding author: Christopher Thomas Williams, ctwilliams@stanford.edu

(Received 27 January 2025; revised 3 June 2025; accepted 8 July 2025)

Turbulence–chemistry interaction in a Mach-7 hypersonic boundary layer with significant production of radical species is characterised using direct numerical simulation. Overriding a non-catalytic surface maintained as isothermal at 3000 K, the boundary layer is subject to finite-rate chemical effects, comprising both dissociation/recombination processes as well as the production of nitric oxide as mediated by the Zel'dovich mechanism. With kinetic-energy dissipation giving rise to temperatures exceeding 5300 K, molecular oxygen is almost entirely depleted within the aerodynamic heating layer, producing significant densities of atomic oxygen and nitric oxide. Owing to the coupling between turbulence-induced thermodynamic fluctuations and the chemical-kinetic processes, the Reynolds-averaged production rates ultimately depart significantly from their mean-field approximations. To better characterise this turbulence–chemistry interaction, which arises primarily from the exchange reactions in the Zel'dovich mechanism, a decomposition for the mean distortion of finite-rate chemical processes with respect to thermodynamic fluctuations is presented. Both thermal and partial-density fluctuations, as well as the impact of their statistical co-moments, are shown to contribute significantly to the net chemical production rate of each species. Dissociation/recombination processes are confirmed to be primarily affected by temperature fluctuations alone, which yield an augmentation of the molecular dissociation rates and reduction of the recombination layer's off-wall extent. While the effect of pressure perturbations proves largely negligible for the mean chemical production rates, fluctuations in the species mass fractions are shown to be the primary source of turbulence–chemistry interaction for the second Zel'dovich reaction, significantly modulating the production of all major species apart from molecular nitrogen.

Key words: high-speed flow, hypersonic flow, turbulent reacting flows

1. Introduction

The conversion of bulk kinetic energy into molecular thermal motion via shock-induced compression and viscous dissipation activates a number of temperature-dependent thermochemical processes within the shock layers of high-speed flight vehicles (Anderson 2006; Bertin & Cummings 2006; Urzay 2018; Urzay & Di Renzo 2021). These high-enthalpy effects include the activation of additional internal degrees of freedom in the form of vibrational and electronic excitation, together with the initiation of chemical reactions among the atomic and molecular components of high-temperature air (Vincenti & Krüger 1965; Park 1990; Zel'Dovich & Raizer 2002). Owing to the comparable characteristic time scales of hydrodynamic motion and thermochemical relaxation in hypersonic flows, the composition within high-Mach boundary layers cannot generally be equated to the minimum-free-energy chemical configuration (Lee 1984; Gnoffo, Gupta & Shinn 1989; Candler 2019). Due to this thermochemical non-equilibrium, the local chemical composition intrinsically depends on the relative rates of advective transport and chemical production, even in the case of laminar hypersonic boundary layers (Inger 1964; Liñán & Da Riva 1962; Seror *et al.* 1997; Williams *et al.* 2021). With the introduction of boundary-layer disturbances to high-enthalpy flows, exchange of chemical and sensible enthalpy by chemical heat release, as well as internal-energy exchange via vibrational relaxation, modifies the stability characteristics of high-Mach flows in terms of both growth rates and frequencies associated with instabilities (Stuckert & Reed 1994; Hudson, Chokani & Candler 1997; Fujii & Hornung 2003; Lyttle & Reed 2005; Germain & Hornung 1997; Marxen, Iaccarino & Magin 2014; Miró *et al.* 2019; Passiatore *et al.* 2024). In addition to distorting the base flow relative to an equivalent calorically perfect boundary layer, high-enthalpy processes likewise have been shown through numerical experiments to impact disturbance amplification itself (Johnson, Seipp & Candler 1998; Knisely & Zhong 2019). Ultimately, the complex interplay between thermochemical effects and the growth of unstable modes are sensitive to both the particular base flow and instability itself, with exchanges among chemical and sensible enthalpies able to either stabilise or destabilise high-enthalpy boundary layers (Bertolotti 1998; Johnson *et al.* 1998; Kline, Chang & Li 2018; Mortensen 2018).

The coupling between the hydrodynamic and thermochemical fields is further complicated by the introduction of a multiplicity of hydrodynamic spatial and temporal scales upon breakdown to turbulence, with flow-induced fluctuations in thermodynamic-state variables directly modulating the mean rates of non-equilibrium thermochemical processes (Duan, Beekman & Martin 2011; Di Renzo & Urzay 2021; Urzay & Di Renzo 2021). As in isotropic turbulence (Martin & Candler 1998, 1999), thermal fluctuations within high-Mach boundary layers give rise to enhancement of dissociation processes (Duan & Martin 2009; Duan & Martín 2011), which correspondingly modifies both the mean-flow thermodynamics and fluctuation statistics. Correspondingly, the chemical heat release associated with exothermic processes has been shown to amplify turbulence kinetic energy and thermal variance in high-Mach turbulence, while both internal-energy excitation and chemical dissociation effectively damp temperature fluctuations owing to their endothermicity (Martin & Candler 2000, 2001; Duan & Martin 2009; Di Renzo, Williams & Pirozzoli 2024). In addition to this mutual interaction between dissociation/recombination chemistry and macroscale hydrodynamic fluctuations, the production of radical species by high-temperature reactions and subsequent mixing by boundary-layer turbulence ultimately imparts significant distortions to the mean reaction rates of the Zel'dovich mechanism. The present manuscript characterises this turbulence–chemistry interaction associated with the shuffle reactions, while also assessing the

relative importance of compositional and thermal mixing for all chemical-kinetic processes.

Together with the emergence of finite-rate thermochemical processes, significant wall-normal thermal variation itself, as arising from viscous dissipation, represents a distinguishing characteristic of high-Mach turbulence. While this aerodynamic heating effect ultimately distorts the turbulence statistics relative to an incompressible boundary layer (Guarini *et al.* 2000; Pirozzoli, Grasso & Gatski 2004; Duan, Beekman & Martin 2010; Duan *et al.* 2011; Pirozzoli & Bernardini 2011), for adiabatic boundary layers or weakly diabatic flows at moderate Mach numbers, the distortions in the mean-flow velocity are largely attributable to mean variations in density and molecular transport properties alone (van Driest 1956; Zhang *et al.* 2012; Patel, Boersma & Pecnik 2016; Trettel & Larsson 2016; Griffin, Fu & Moin 2021). For diabatic high-Mach boundary layers, however, intrinsic-compressibility effects (Lele 1994; Smits & Dussauge 2006; Yu, Xu & Pirozzoli 2019) have been shown to emerge in violation of Morkovin's hypothesis (Morkovin 1962; Bradshaw 1977), associated not only with modulation of pressure fluctuations in the viscous sublayer (Yu, Xu & Pirozzoli 2020) but the mean-velocity profile itself (Hasan *et al.* 2023, 2024). With the activation of chemical reactions in high-Mach wall-bounded flows, pressure perturbations directly modulate the rate of dissociation/recombination processes, and yet, the significance of this intrinsic compressibility as it pertains to turbulence-aerothermochemistry interactions remains uncharacterised.

The objective of this paper is to systematically characterise turbulence–aerothermochemistry interactions in a spatially evolving turbulent reacting hypersonic boundary layer, with particular focus on analysing the effects of species mixing and temperature fluctuations on the Zel'dovich mechanism. To that end, direct numerical simulation results of a high-enthalpy Mach-7 turbulent hypersonic boundary layer, with significant chemical production of radical species, are presented. In order to disambiguate the effects of thermal and compositional fluctuations in high-Mach turbulence–chemistry interaction, a computational approach for statistical decomposition of the expected rates of chemical processes with respect to specific thermodynamic fluctuations is applied to the boundary-layer simulation and, finally, leveraged to assess the impact of pressure perturbations on species production in wall-bounded turbulent hypersonic flows.

The remainder of this manuscript is structured as follows. First, the overall physical configuration for the direct numerical simulation is presented in § 2. The relevant conservation equations, treatment of molecular transport and chemical kinetics, as well as additional details of the computational approach utilised for the direct numerical simulation, are presented in § 3. The corresponding mean-flow results for the turbulent boundary-layer simulation, together with the statistical decompositions of turbulence–chemistry interaction in terms of both chemical production and reaction rates, are presented in § 4. Finally, concluding remarks are provided § 5, while further description of the laminar base flow (Appendix A), verification of the turbulent state (Appendix B), assessment of grid convergence (Appendix C) and additional species-specific decompositions for turbulence–chemistry interaction (Appendix D) are deferred to the appendices.

2. Physical configuration

The direct numerical simulation is performed in a Cartesian computational domain with the incoming laminar boundary-layer profile obtained from an auxiliary two-dimensional simulation of the reacting hypersonic flow over a 16° wedge at a free-stream Mach

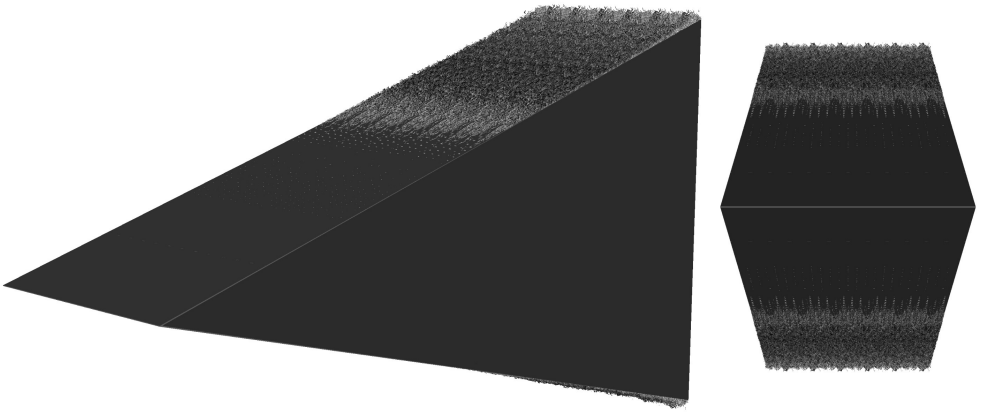

Figure 1. Composite schematic of the overall physical configuration consisting of the auxiliary inflow calculation together with the Cartesian boundary-layer simulation, reflected across the wedge midplane. Six spanwise periods of the primary simulation domain depict the breakdown to turbulence.

number of 25; a schematic of this overall configuration is provided in figure 1. This approach enables leading-edge effects to be fully captured, producing heightened levels of atomic nitrogen in the boundary layer relative to a locally self-similar approximation (Lees 1956; Di Renzo & Urzay 2021). Compression from the nose shock wave produces an inviscid shock layer with a Mach number of 7.0 and a temperature of 2686 K, corresponding to the edge conditions for the boundary layer itself. The wall in both the hypersonic wedge and boundary-layer calculations is treated consistently as isothermal and non-catalytic with a temperature of 3000 K. Although not uncharacteristic of high-Mach atmospheric re-entry, this elevated surface temperature would likely give rise to gas–surface interaction for a realistic thermal protection system. Modification of gas-phase turbulence–chemistry interaction in hypersonic boundary layers by surface chemical effects will therefore be addressed therefore in a subsequent study. Further discussion of the auxiliary wedge calculation and presentation of the corresponding laminar boundary-layer profiles are provided in Appendix A. Following breakdown to turbulence, the friction Knudsen number (McMullen *et al.* 2023) for the turbulent reacting boundary layer remains below 1.5×10^{-3} throughout the entire simulation domain, evidencing the self-consistency of the continuum formulation utilised in the present study. The vibrational Damköhler numbers based on the Landau–Teller relaxation constant (Landau & Teller 1936; Millikan & White 1963; Park 1990, 1993), evaluated with the mean thermodynamic variables at the peak-temperature location, and the eddy-turnover time scale remain above 2.9×10^{1}, 9.8×10^{2}, and 6.3×10^{2} for molecular nitrogen, nitric oxide and molecular oxygen, respectively, consistent with the thermal-equilibrium formulation utilised for this investigation.

3. Formulation

3.1. *Conservation equations*

On account of the finite-rate evolution of the chemical state variables in hypersonic flows, determination of the local composition entails integration of a partial-density conservation equation for each of the components, given by

$$\frac{\partial(\rho Y_i)}{\partial t} + \boldsymbol{\nabla} \cdot (\rho Y_i \boldsymbol{u}) = -\boldsymbol{\nabla} \cdot (\rho Y_i \boldsymbol{V_i}) + \dot{w}_i \quad i = 1, \ldots, N_s, \tag{3.1}$$

where ρ and $\boldsymbol{u} = [u,\ v,\ w]^{\mathrm{T}}$ are the overall density and mass-averaged velocity of the reacting mixture, respectively. The mass fraction for a given species i is denoted by Y_i, whereas $\boldsymbol{V_i}$ is defined as the corresponding diffusion velocity, and $\dot{w}_i$ is taken to be the net chemical production rate per unit volume. The diffusion velocities are determined as (Curtiss & Hirschfelder 1949; Coffee & Heimerl 1981; Ern & Giovangigli 1994)

$$\boldsymbol{V_i} = -D_i \nabla \ln X_i + \sum_{j=1}^{N_s} Y_j D_j \nabla \ln X_j, \tag{3.2}$$

where $X_i = \mathcal{M} Y_i / \mathcal{M}_i$ and D_i, respectively, correspond to the molar fraction of, and to the mixture-averaged mass diffusivity (Bird, Stewart & Lightfoot 1960) for, species i. In this formulation, the molar mass of species i is given by $\mathcal{M}_i$, whereas $\mathcal{M} = [\sum_{i=1}^{N_s} Y_i / \mathcal{M}_i]^{-1}$ denotes the effective molar mass of the mixture. The present study utilises the Park (1990) chemical mechanism for air dissociation given by

$$\mathrm{N_2 + O \rightleftharpoons NO + N}, \tag{R1}$$
$$\mathrm{NO + O \rightleftharpoons O_2 + N}, \tag{R2}$$
$$\mathrm{O_2 + M \rightleftharpoons 2O + M}, \tag{R3}$$
$$\mathrm{NO + M \rightleftharpoons N + O + M}, \tag{R4}$$
$$\mathrm{N_2 + M \rightleftharpoons 2N + M}, \tag{R5}$$

comprising the Zel'dovich exchange reactions, (R1) and (R2), together with the dissociation/recombination reactions for each of the diatomic species species given by (R3)–(R5). The reactive mixture is composed of five species, i.e. $N_s = 5$, with the symbolic species M representing the third-body collision partners entering into the dissociation/recombination reactions. As such, accounting for all collision partners, the total number of reactions considered is $N_r = 17$. With a peak mean temperature of approximately five thousand Kelvin in the turbulent portion of the boundary layer, the consideration of neutral chemistry alone is warranted for the present study, although accurate characterisation of turbulence–chemistry interaction in higher temperature and less collisional flows may, however, demand state-resolved modelling of kinetic processes (Capitelli, Armenise & Gorse 1997; Panesi *et al.* 2009, 2014).

In terms of the reaction rates, $\mathcal{R}_i$, the chemical production rates merely represent a linear combination with $\dot{w}_i = \mathcal{M}_i \sum_{j=R_1}^{R_5} (\nu''_{ij} - \nu'_{ij}) \mathcal{R}_j$. Following from the law of mass action, then, the net chemical production term for species i can then be evaluated as

$$\dot{w}_i = \mathcal{M}_i \sum_{j=R_1}^{R_5} \left(\nu''_{ij} - \nu'_{ij}\right) \sum_{l=1}^{N_s} F_{lj} \left[k_{f,j} \prod_{k=1}^{N_s} \left(\frac{\rho Y_i}{\mathcal{M}_i}\right)^{\nu'_{kj}} - \frac{k_{f,j}}{K_{eq,j}} \prod_{k=1}^{N_s} \left(\frac{\rho Y_i}{\mathcal{M}_i}\right)^{\nu''_{kj}} \right], \tag{3.3}$$

where F_{lj} is a chaperon efficiency function of the third-body collision partner l in reaction j, while $\nu'_{kj}, \nu''_{kj} \in \mathbb{N}$, respectively, correspond to the forward and reverse stoichiometric coefficients for species k in elementary reaction j. The modified-Arrhenius rate constants for each of the reactions in the forward direction are given by

$$k_{f,j} = A_j T^{m_j} \exp\left(-\frac{E_{a,j}}{R^0 T}\right), \quad j = 1, \ldots, N_r, \tag{3.4}$$

where R^0 denotes the universal gas constant, and A_j, m_j and $E_{a,j}$ are the Arrhenius parameters provided by Park (1989). The chemical equilibrium constants $K_{eq,j}$ are

evaluated with

$$K_{eq,j} = \exp\left(-\sum_{k=1}^{N_s}(\nu''_{kj} - \nu'_{kj})\frac{\mathcal{G}_k}{R^0 T}\right)\left(\frac{P_0}{R^0 T}\right)^{\sum_{i=1}^{N_s}\left(\nu''_{ij}-\nu'_{ij}\right)}, \tag{3.5}$$

where $\mathcal{G}_k$ is the Gibbs free energy of species k, evaluated at the reference pressure P_0. For the present study, the Gibbs free energy for each species is evaluated with the parameterisation of McBride, Zehe & Gordon (2002); therefore, P_0 is taken to be 100 kPa. In this continuum formulation, the conservation of momentum implies the compressible Navier–Stokes equations as given by

$$\frac{\partial(\rho \boldsymbol{u})}{\partial t} + \boldsymbol{\nabla} \cdot (\rho \boldsymbol{u}\boldsymbol{u}) = -\boldsymbol{\nabla} P + \boldsymbol{\nabla} \cdot \overline{\overline{\boldsymbol{\tau}}}, \tag{3.6}$$

where the ideal-gas equation of state relates the pressure P to the thermodynamic temperature T as

$$P = \rho R^0 T / \mathcal{M}. \tag{3.7}$$

Consistent with Stokes' hypothesis (Valentini, Grover & Bisek 2024), the viscous stress tensor may be expressed in terms of the strain-rate tensor $\overline{\overline{\boldsymbol{S}}} = (\boldsymbol{\nabla}\boldsymbol{u} + \boldsymbol{\nabla}\boldsymbol{u}^T)/2$ and identity tensor $\overline{\overline{\boldsymbol{I}}}$ as

$$\overline{\overline{\boldsymbol{\tau}}} = 2\mu\overline{\overline{\boldsymbol{S}}} - \frac{2\mu}{3}(\boldsymbol{\nabla} \cdot \boldsymbol{u})\,\overline{\overline{\boldsymbol{I}}}, \tag{3.8}$$

where μ is the dynamic viscosity of the mixture. For the present study, μ is determined from Wilke's mixture rule (Wilke 1950) for which the elementary viscosity of each species is evaluated following the approach of Curtiss & Hirschfelder (1949). The corresponding conservation equation for the total energy is

$$\frac{\partial(\rho E)}{\partial t} + \boldsymbol{\nabla} \cdot (\rho E \boldsymbol{u}) = \boldsymbol{\nabla} \cdot \left(-\boldsymbol{u} P + \overline{\overline{\boldsymbol{\tau}}}\boldsymbol{u} + \lambda \boldsymbol{\nabla} T - \rho \sum_{i=1}^{N_s} Y_i \boldsymbol{V_i} h_i\right), \tag{3.9}$$

where λ is the effective thermal conductivity determined from the mixing rule of Mathur, Tondon & Saxena (1967), with the thermal conductivity of each component evaluated following the approach of Peters & Warnatz (2013). The stagnation energy E comprises contributions from specific kinetic energy and internal energy as $E = (\boldsymbol{u} \cdot \boldsymbol{u})/2 + e$. The internal energy itself accounts for both excitation of thermal motion and chemical energy stored in molecular bonds with

$$e = \sum_{i=1}^{N_s} Y_i h_i - P/\rho, \tag{3.10}$$

where h_i is the specific enthalpy of species i, evaluated with the polynomial description of McBride *et al.* (2002). This set of conservation equations as formulated above is integrated numerically with the HTR solver (Di Renzo, Fu & Urzay 2020) for direct numerical simulation of the Mach-7 turbulent reacting hypersonic boundary layer. The inviscid fluxes are evaluated with a low-dissipation, sixth-order hybrid skew–symmetric/targeted essentially non-oscillatory scheme (Pirozzoli 2010; Fu, Hu & Adams 2016; Williams, Di Renzo & Moin 2022), while explicit time advancement is performed using a third-order strong-stability-preserving Runge–Kutta method (Gottlieb, Shu & Tadmor 2001).

3.2. *Computational approach*

The primary simulation domain for the direct numerical simulation extends a length of $800\delta_0^*$, $14\pi\delta_0^*$ and $40\delta_0^*$ in the streamwise, spanwise and wall-normal directions, respectively, where δ_0^* is the displacement thickness of the incoming laminar boundary layer. The streamwise coordinate x is measured from the leading edge of the wedge and hence $x \in [x_0, x_0 + 800\delta_0^*]$, where $x_0 = 117\delta_0^*$ is the distance along the wedge surface from the leading edge at which the laminar boundary layer is extracted. The computational domain is discretised with 11 868, 1184 and 464 points in the streamwise, spanwise and wall-normal directions, respectively, with a uniform distribution of points employed in the streamwise and spanwise coordinates. Along the wall-normal coordinate, the points are stretched as $\hat{y}_j = 40\sinh(s\xi_j)/\sinh(s)$, with $\widehat{(\cdot)}$ denoting normalisation by δ_0^*. The stretching factor, s, is set equal to 5.0, and $\xi_j \in [0, 1]$ is a uniformly spaced computational coordinate.

Transition to turbulence is induced by unsteady suction and blowing at the wall, which is applied a distance of $15\delta_0^*$ downstream of the inflow boundary, across a strip with a streamwise extent $5\delta_0^*$. The forcing employed for the present study has the same functional form as that of Franko & Lele (2013) and Di Renzo & Urzay (2021), for which a non-zero vertical velocity is imposed at the wall, namely, $v = f(x)g(z)\sum_{i=1}^{2} A_i sin(\omega_i t - \beta_i z)$, where A_i, ω_i and β_i naturally correspond to the amplitude, frequency and spanwise wavenumber of the ith mode. The functions $f(x) = \exp[-(x/\delta_0^* - x_s/\delta_0^*)^2/1.125]$ and $g(z) = 1.0 + 0.1\{\exp\{-[(z - z_c - z_l)/z_l]^2\} + \exp\{-[(z - z_c + z_l)/z_l]^2\}\}$ provide streamwise localisation and spanwise asymmetry within the forcing strip, where $x_s = x_0 + 17.5\delta_0^*$, $z_c = 7\pi\delta_0^*$ and $z_l = 1.4\pi\delta_0^*$. For the present study, two modes are introduced, each with an amplitude set to 5.0 % of the edge streamwise velocity, U_e. The spanwise wavenumbers for the forcing modes are $\pm 2/(7\delta_0^*)$, each with a temporal frequency of $9a_e/(10\delta_0^*)$, where a_e is the speed of sound at the edge of the boundary. Finally, periodicity is enforced in the spanwise direction, while characteristic boundary conditions are applied along the outflows located at $\hat{x} = x_0/\delta_0^* + 800$ and $\hat{y} = 40$. Statistical convergence is achieved by averaging in time and along the homogeneous direction over the course of 10 eddy turnovers, sampling the solution fields once every 10 time steps. In terms of notation, this Reynolds-averaging operator is denoted by $\overline{(\cdot)}$, while the Favre/density-weighted averaging operator is represented with $\widetilde{(\cdot)} = \overline{\rho(\cdot)}/\overline{\rho}$; fluctuations relative to Reynolds-averaged and Favre-averaged variables will meanwhile be denoted with $(\cdot)'$ and $(\cdot)''$, respectively.

4. Results

Breakdown to turbulence in the Mach-7 reacting hypersonic boundary layer strongly modulates the rate of chemical reactions and compositional structure of the boundary layer. Figure 2(*a*) depicts the Q-criterion (Hunt, Wray & Moin 1988) isosurfaces coloured by the local molecular-oxygen molar fraction during the laminar-to-turbulent transition, together with contours of the normalised density gradient to visualise the radiated acoustic waves. Figure 2(*b*) evidences the strong variation in nitric oxide concentration through the transition process, owing to the enhanced turbulent mixing of thermodynamic states between the lower-temperature largely undissociated air at the boundary-layer edge and the strongly reacting near-wall mixture in the aerodynamic heating layer. Streamwise planes of the molar fractions for each species in the fully turbulent region are depicted in figure 3 reflecting this significant compositional non-uniformity and turbulence-induced species mixing. The mean molar fractions of dissociated species at the non-catalytic wall

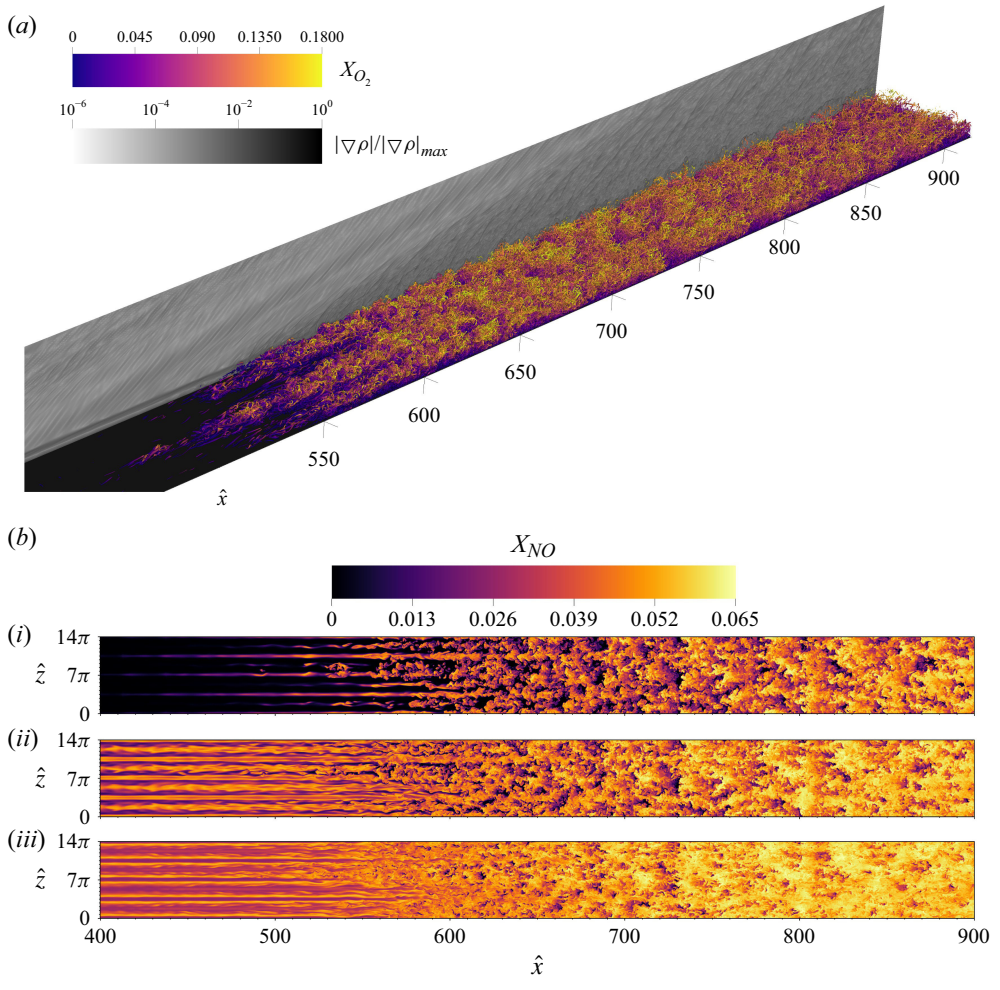

Figure 2. (*a*) Isosurface of the Q-criterion coloured by the molar fraction of molecular oxygen, with the side panel depicting contours of the density-gradient magnitude. (*b*) Instantaneous contours of the nitric oxide molar fraction at the three off-wall locations corresponding to (i) $\hat{y} = 3.0$, (ii) $\hat{y} = 2.0$ and (iii) $\hat{y} = 1.0$.

itself are provided in table 1 for a few streamwise locations, together with the normalised grid spacing in viscous units and the set of dimensionless parameters characterising the hydrodynamics of the turbulent reacting boundary layer.

4.1. *Velocity, density and temperature statistics*

The transformed mean-velocity profiles as a function of the semi-local coordinate (Huang, Coleman & Bradshaw 1995; Trettel & Larsson 2016; Griffin *et al.* 2021) $y^* = y(\sqrt{\tau_w \overline{\rho}})/\overline{\mu}$ are depicted in figure 4, together with the second-order velocity-fluctuation statistics. The mean-velocity data from the present calculation exhibit a close collapse onto the incompressible scaling under the intrinsic-compressibility transformation of Hasan *et al.* (2023). Consistent with prior numerical simulations of calorically perfect (Zhang, Duan & Choudhari 2018; Cogo *et al.* 2022; Huang, Duan & Choudhari 2022; Huang *et al.* 2022) and weakly reactive (Duan & Martín 2011; Di Renzo & Urzay 2021; Passiatore *et al.* 2022) high-speed turbulent boundary layers, both the turbulent Mach number,

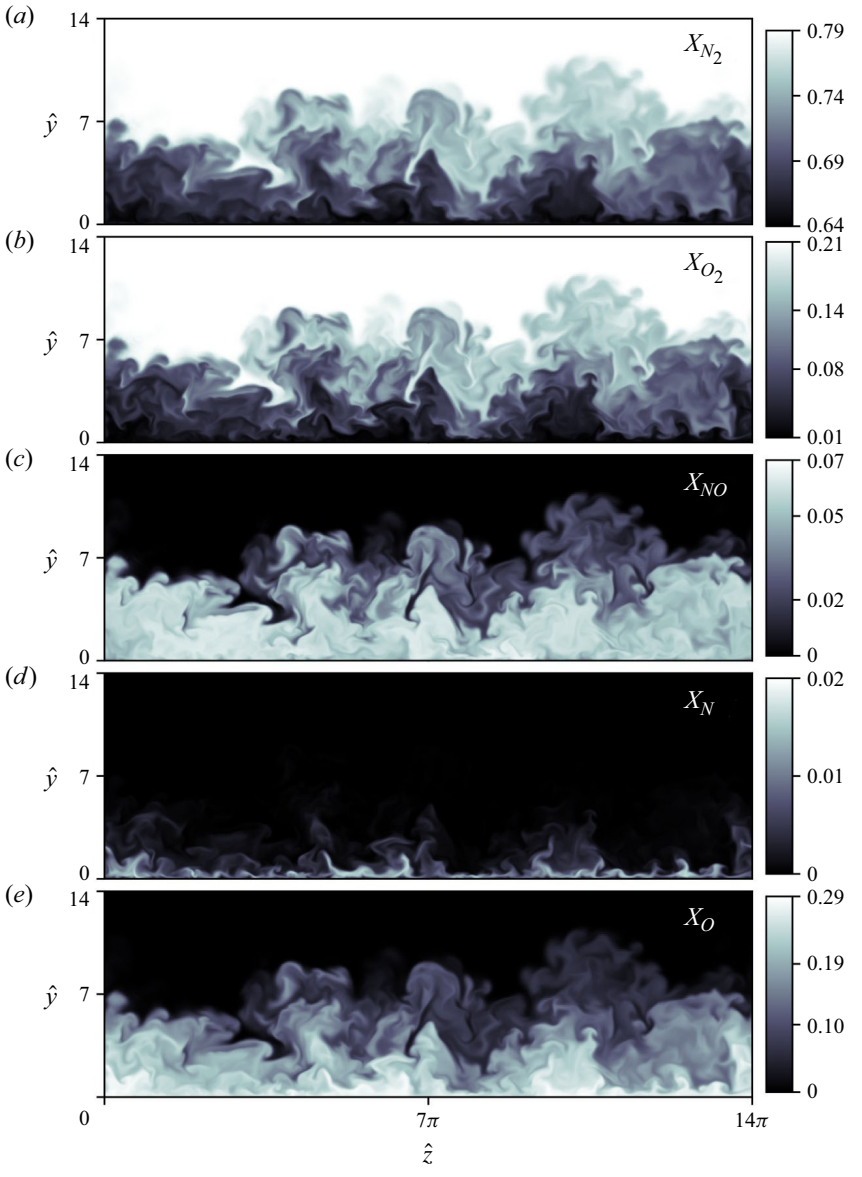

Figure 3. Molar-fraction contours along the streamwise-normal plane at $\hat{x} = 916$. The panels correspond to the molar fractions of (*a*) molecular nitrogen, (*b*) molecular oxygen, (*c*) nitric oxide, (*d*) atomic nitrogen and (*e*) atomic oxygen, respectively.

$Ma_t = \sqrt{(\boldsymbol{u} \cdot \boldsymbol{u})/3}/\overline{a}$, and streamwise-normal component of the Reynolds-stress tensor attain their maxima just outside the peak-mean-temperature location and within the buffer layer at $y^* \simeq 20$, corresponding to a peak turbulent Mach number of $Ma_t \simeq 0.7$. The wall-normal and spanwise normal components of the Reynolds stresses, as well as the Reynolds shear, in contrast reach their maxima further from the wall at semi-local distances of the order of $y^* \simeq 100$. Viscous dissipation of kinetic energy in the boundary layer ultimately gives rise to an aerodynamic heating layer with a peak temperature $\simeq 5300$ K at an off-wall location of $y^* \simeq 10$, activating significant dissociation/recombination phenomena and production of nitric oxide via the Zel'dovich mechanism. The presence of significant

$\hat{x} = x/\delta_0^*$	700	750	800	850	900
$\hat{\delta}$	6.31	7.02	7.62	8.18	8.75
$\overline{h}_w/\overline{h}_r$	4.08	4.07	4.05	4.03	4.01
$C_f(\times 10^2)$	0.18	0.17	0.17	0.16	0.16
$C_q(\times 10^3)$	−0.41	−0.39	−0.38	−0.37	−0.36
Re_τ	905	985	1051	1110	1175
Ma_τ	0.21	0.20	0.20	0.19	0.19
Re_{δ_2}	1984	2256	2446	2611	2836
Re_θ	2210	2516	2723	2901	3155
Ec	2.61	2.61	2.62	2.62	2.62
$\widetilde{X}_{NO,w}(\times 10^2)$	4.81	4.84	4.79	4.66	4.57
$\widetilde{X}_{N,w}(\times 10^2)$	0.32	0.29	0.29	0.29	0.29
$\widetilde{X}_{O,w}$	0.26	0.26	0.26	0.27	0.27
Δx^+	9.68	9.46	9.30	9.14	9.05
Δz^+	5.33	5.21	5.12	5.04	4.99
Δy_w^+	0.83	0.82	0.80	0.79	0.78
Δy_δ^+	9.77	10.63	11.39	11.94	12.74

Table 1. Dimensionless parameters at select streamwise locations based on the averaged primitive variables. Normalised by the inflow displacement thickness, $\hat{\delta}$ is the height at which the Favre-averaged velocity recovers 99 % of the edge streamwise velocity. The mean wall-to-recovery enthalpy ratio $\overline{h}_w/\overline{h}_r$ is evaluated as $h_r = h_e + rU_e^2/2$ with a recovery factor of $r = 0.9$ (Gibis *et al.* 2024). The skin-friction and heat-flux coefficients are given by $C_f = 2\tau_w/\rho_e U_e^2$ and $C_q = q_w/\rho_e U_e^3$, where τ_w and q_w are the average wall stress and heat flux, respectively. The friction Reynolds and Mach numbers are defined as $Re_\tau = \overline{\rho}_w u_\tau \delta/\overline{\mu}_w$ and $Ma_\tau = u_\tau/\overline{a}_w$, respectively, where $\overline{a}_w$ is the mean sound speed at the wall. The Reynolds numbers based on the momentum thickness θ are likewise defined as $Re_{\delta_2} = \rho_e U_e \theta/\mu_w$ and $Re_\theta = \rho_e U_e \theta/\mu_e$. The Eckert number is given by $Ec = U_e^2/(\overline{h}_w - \overline{h}_r)$, while the Favre-averaged mole fractions of reaction products at the wall are denoted as $\widetilde{X}_{i,w}$. Finally, the grid-spacing dimensions in friction units for the streamwise and spanwise directions, together with the wall-normal spacing as evaluated at the wall and at $y = \delta$, are denoted by Δx^+, Δz^+, Δy_w^+ and Δy_δ^+, respectively.

aerodynamic heating is apparent in both the density-weighted average temperature and Reynolds-averaged density fields, which are characterised in figure 5, with the peak-temperature location naturally corresponding to a global minimum for the mean density. The root-mean-squares (r.m.s.) of density fluctuations and density-weighted temperature fluctuations, as normalised by the local mean value, are likewise represented in figure 5, each realising a local minimum in the vicinity of the temperature peak itself. Within the peak-temperature location, whereas the normalised r.m.s. of density fluctuations increases monotonically with decreasing wall-normal displacement, the normalised r.m.s. of the density-weighted thermal fluctuations exhibits a local maximum in the viscous sublayer at $y^* \simeq 4$. The emergence of this near-wall thermal-variance peak is consistent with a turbulent-transport mechanism associated with the combined presence of strong near-wall temperature gradients and inviscid transport of temperature fluctuations away from the temperature peak (Fan, Li & Pirozzoli 2022; Cogo *et al.* 2023*a*), although owing to the presence of chemical non-equilibrium, the balance of thermal variance is mediated not only by convective and conductive processes but also by chemical-heat-release and species-diffusion effects (Martin & Candler 2001).

4.2. *Species-production-rate and chemical-composition statistics*

The high temperatures in the aerodynamic heating layer ultimately yield significant variations in the boundary layer's chemical composition, depleting essentially all molecular

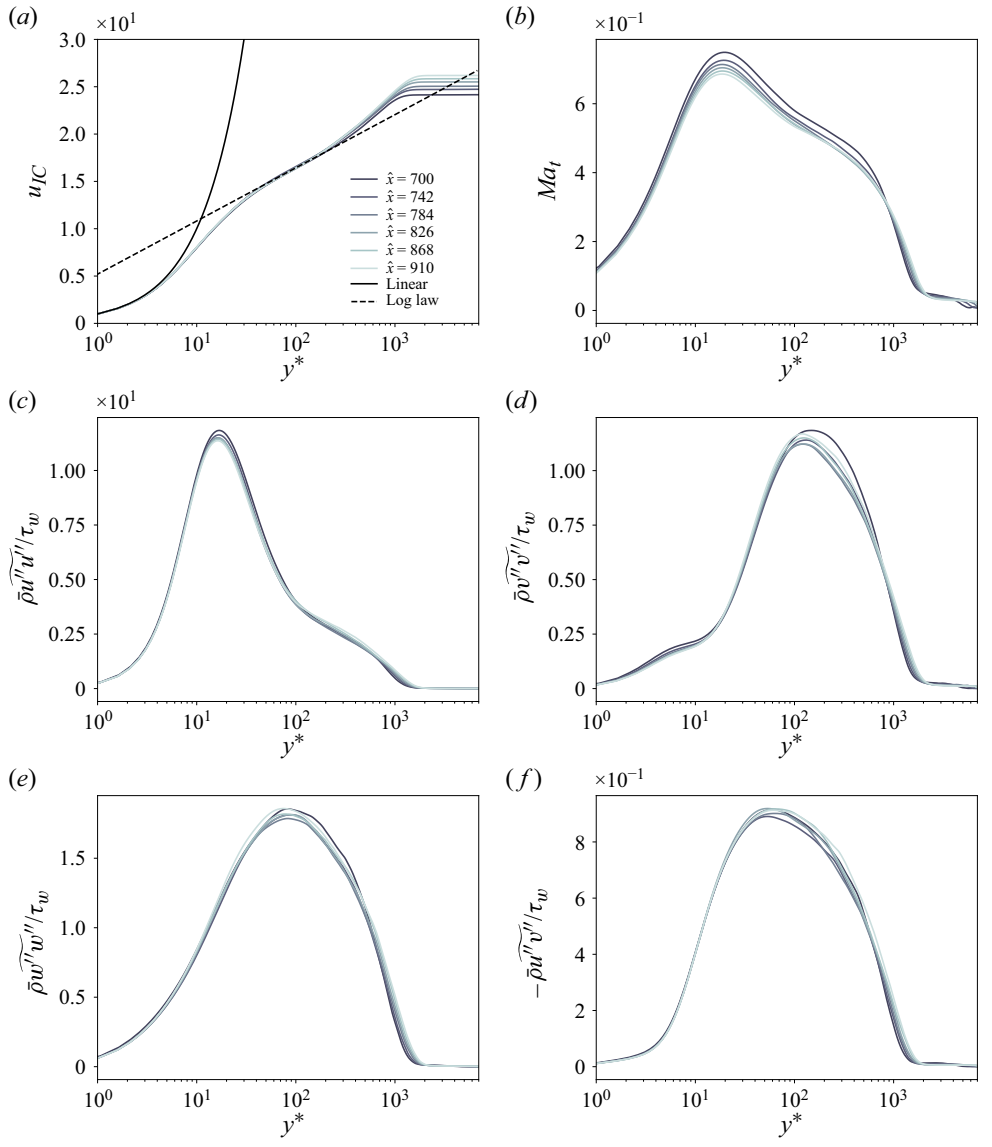

Figure 4. (*a*) Transformed mean-velocity profiles utilising intrinsic-compressibility transformation of Hasan *et al.* (2023), u_{IC}, together with wall-normal variation in the (*b*) turbulent Mach number, diagonal elements of the Reynolds-stress tensor corresponding to the (*c*) streamwise, (*d*) wall-normal and (*e*) spanwise directions and (*f*) Reynolds shear stress. Further characterisations of the van Driest (1956) and Griffin *et al.* (2021) mean-velocity transformations are provided in Williams, Di Renzo & Moin (2023).

oxygen within the peak-temperature location and producing measurable concentrations of nitric oxide, atomic oxygen and atomic nitrogen. Characterising the spatial evolution of the compositional statistics, the Favre-averaged molar fractions and their corresponding r.m.s. of density-weighted fluctuations are depicted in figures 6 and 7. While the concentrations of dissociation products are negligible at the edge of the boundary layer, the proportion of undissociated nitrogen and oxygen falls significantly in the aerodynamic heating layer, with $\widetilde{X}_{N_2} \simeq 0.65$ and $\widetilde{X}_{O_2} \simeq 0.02$ near the peak-temperature location. This almost-complete dissociation of oxygen produces a peak Favre-averaged molar fraction of 0.27 for

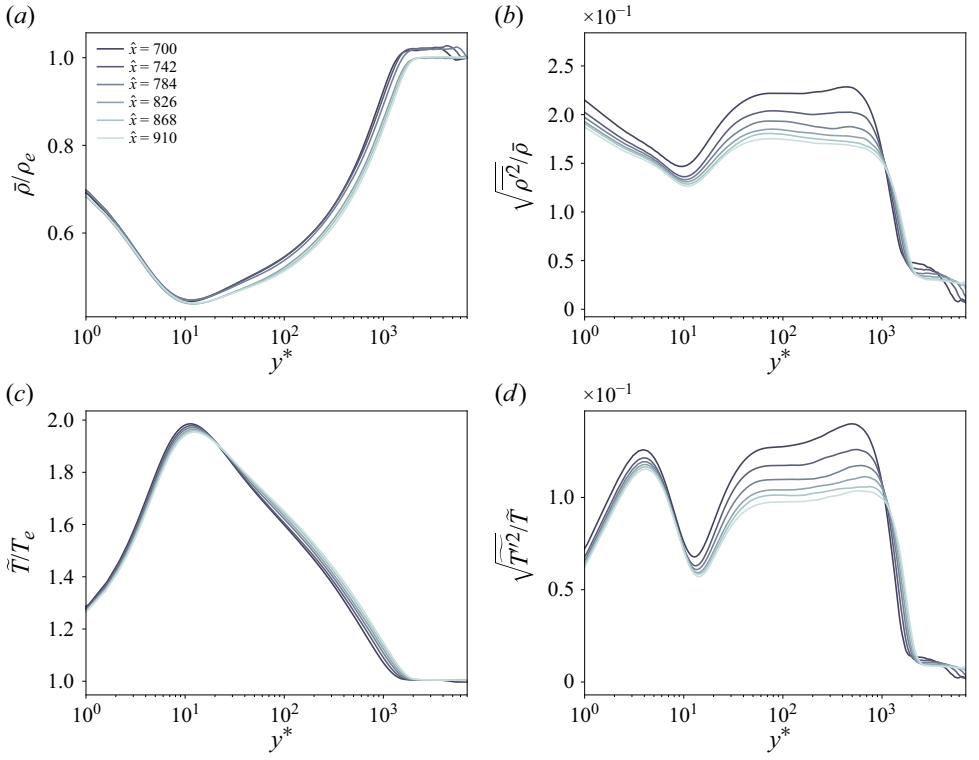

Figure 5. Wall-normal profiles of the (*a*) Reynolds-averaged density, (*b*) r.m.s. of density fluctuations, (*c*) Favre-averaged temperature and (*d*) r.m.s. of density-weighted temperature fluctuations.

atomic oxygen in the vicinity of the non-catalytic wall. Non-negligible densities of atomic nitrogen and nitric oxide also arise in the boundary layer, with maximum molar fractions of approximately 0.06 and 0.01, respectively. Whereas the Favre-averaged molecular-oxygen and atomic-oxygen molar fractions vary monotonically throughout the boundary layer, molecular and atomic nitrogen in contrast exhibit non-monotonicity with local extrema at $y^* \simeq 10$ as a consequence of a sign change in their respective chemical production rates within the peak-temperature location. Mediated by both molecular dissociation and the Zel'dovich mechanism, the average nitric-oxide molar fraction reaches its maximum at an off-wall location embedded within the buffer layer of the turbulent boundary layer. Turbulent mixing of the molar fractions ultimately produces maxima in the r.m.s. of density-weighted molar-fraction fluctuations for all molecular species, as well as for atomic oxygen, at semi-local distances of the order of $y^* \simeq 10^2$ due to transport of reaction products away from the aerodynamic heating layer. For atomic nitrogen, however, the location of maximum variance remains within the high-temperature buffer layer, where in conjunction with species turbulent mixing, the atomic-nitrogen fluctuations are influenced more significantly by fluctuations in the chemical production rate itself.

As implied by the spatial evolution of the molar fractions, significant chemical production of atomic species and nitric oxide transpires in the vicinity of the temperature peak, proceeding on temporal scales comparable to that of eddy turnover, as reflected by the characteristic turbulent Damköhler numbers for the chemical production of each species listed in table 2. As depicted in figure 8, the average chemical production rates for all species exhibit local extrema near the peak-temperature location owing to their

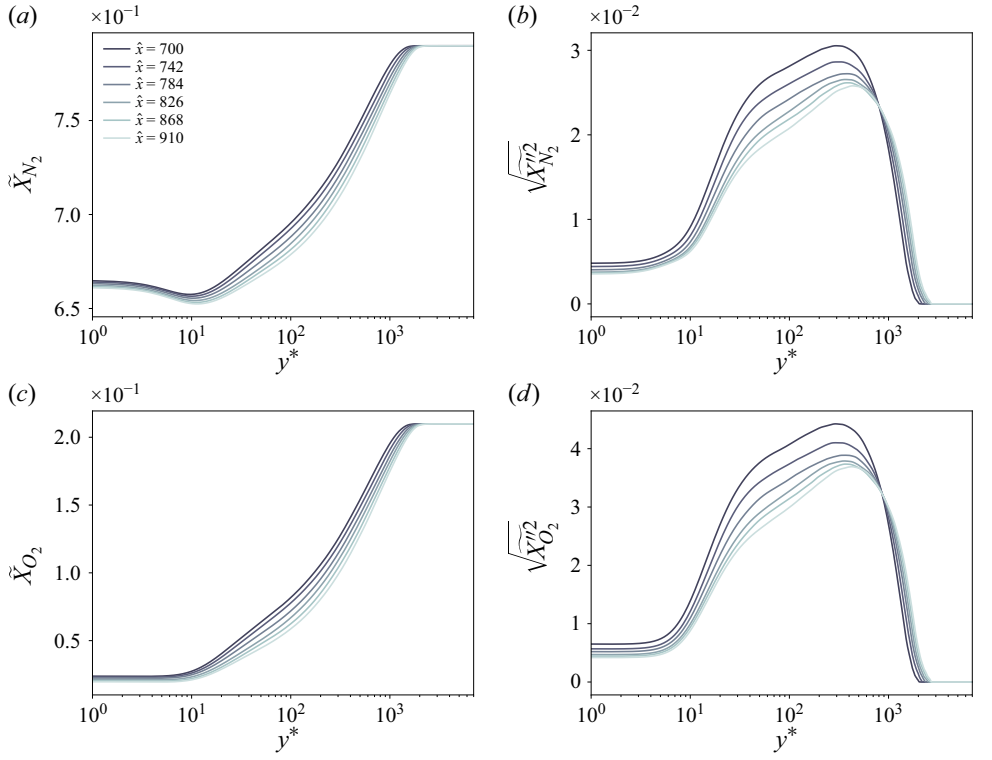

Figure 6. Favre average and r.m.s. of density-weighted fluctuations for the molar fractions of (*a*,*b*) molecular nitrogen, and (*c*, *d*) molecular oxygen, respectively.

strong thermal dependence. In particular, the high temperatures in the vicinity of $y^* \simeq 10$ give rise to significant net positive production of all radical species, NO, N and O, via the consumption of molecular nitrogen and oxygen. Whereas the chemical production of atomic oxygen remains uniformly positive throughout the boundary layer, the chemical production rates of atomic nitrogen and nitric oxide change sign within the temperature peak due to the strong near-wall spatial variation in thermodynamic conditions. The production of nitric oxide and atomic nitrogen becomes negative just within the viscous sublayer at $y^* \simeq 5$ primarily as a result of the Zel'dovich shuffle reactions. This heightened near-wall activity for the shuffle reactions likewise results in the net production rate of molecular nitrogen becoming positive within the viscous sublayer. Finally, while the overall production of atomic oxygen remains positive within the temperature peak due to the Zel'dovich mechanism, the near-wall production of molecular oxygen ultimately becomes positive at sufficiently high Reynolds numbers due to the predominance of its recombination reaction.

4.3. *Thermodynamic decomposition of turbulence/chemistry interaction*

Owing to the nonlinearity of the chemical reaction rates with respect to the fluctuating thermodynamic variables, the Reynolds-averaged chemical production rates

$$\overline{\dot{w}}_i = \int_{\mathbb{R}^{N_s+1}} \mathrm{d}\mathcal{V}\ \dot{w}_i(\{\rho_j\}, T)\mathcal{P}(\{\rho_j\}, T), \tag{4.1}$$

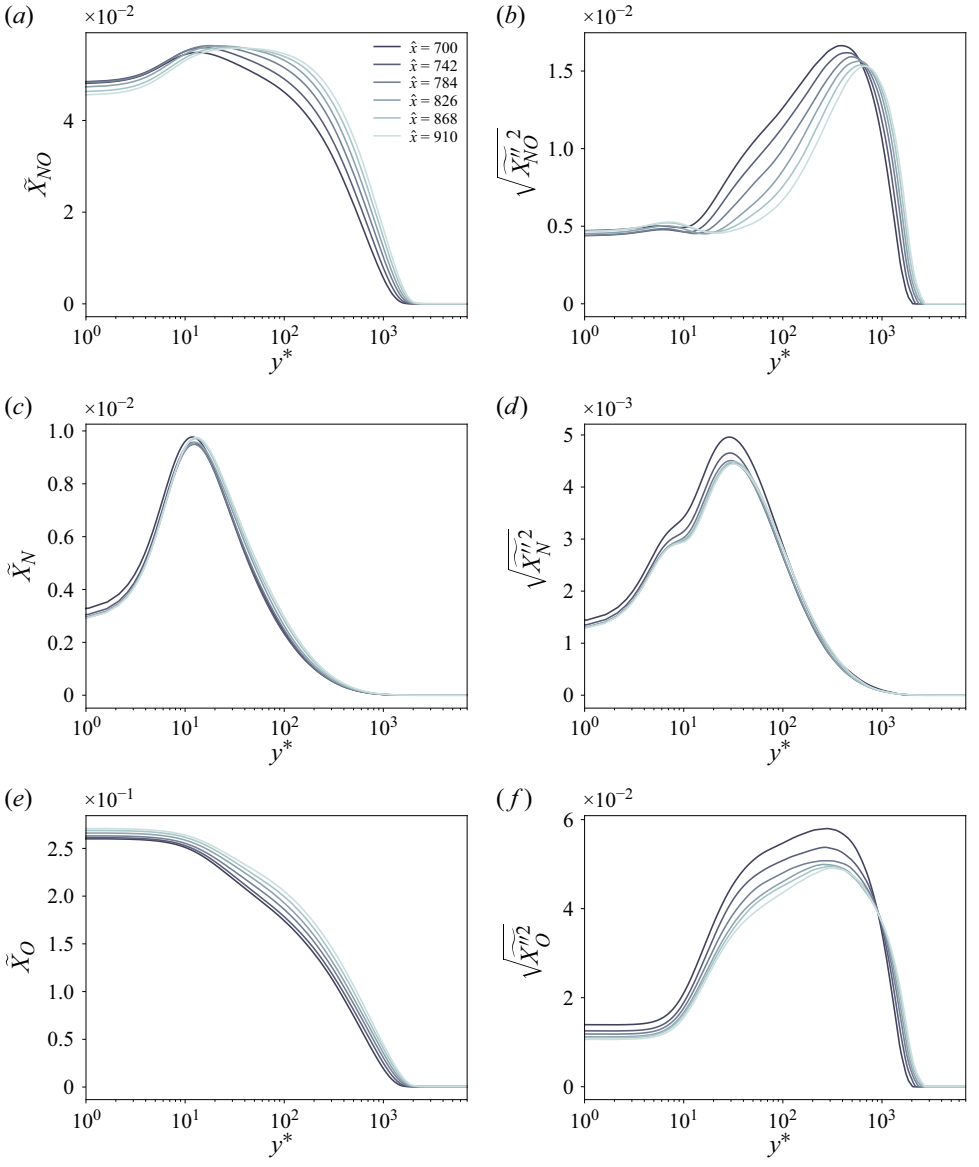

Figure 7. Favre average and r.m.s. of density-weighted fluctuations for the molar fractions of (*a*,*b*) nitric oxide, (*c*, *d*) atomic nitrogen and (*e*, *f*) atomic oxygen, respectively.

may depart significantly from the mean-field approximation given by

$$\dot{w}_i^{mf} = \int_{\mathbb{R}^{N_s+1}} \mathrm{d}\mathcal{V}\ \dot{w}_i(\{\rho_j\}, T)\delta(T - \widetilde{T}) \prod_{\kappa=1}^{N_s} \delta\left(\rho_\kappa - \overline{\rho}_\kappa\right) = \dot{w}_i\left(\{\overline{\rho}_j\}, \widetilde{T}\right), \tag{4.2}$$

where $\mathrm{d}\mathcal{V} = \mathrm{d}T \prod_{\kappa=1}^{N_s} \mathrm{d}\rho_\kappa$ is the differential volume element in thermodynamic-state space, and $\mathcal{P}(\cdot)$ is the single-point (joint) probability density function of the thermodynamic variables taken as arguments. As reflected in figure 9, $\dot{w}_i^{mf}$ differ significantly from $\overline{\dot{w}}_i$ for all species apart from nitric oxide, evidencing the strong

$\hat{x}$	700	750	800	850	900
Da_{t,N_2}	0.43	0.45	0.48	0.51	0.54
Da_{t,O_2}	0.26	0.26	0.25	0.24	0.24
$Da_{t,NO}$	0.40	0.42	0.45	0.48	0.51
$Da_{t,N}$	0.25	0.26	0.27	0.28	0.30
$Da_{t,O}$	0.21	0.22	0.22	0.23	0.24

Table 2. Turbulent Damköhler numbers, $Da_{t,i} = \max(|\overline{\dot{w}}_i/\overline{\rho}|)\delta/u_\tau$, characterising the relative rate of large-scale eddy turnover to chemical production for each species $i = 1, 2, \ldots, N_s$ at $Re_{\delta_2} \simeq 2900$.

interactions between turbulent fluctuations and chemical reactions. In particular, the mean-field approximation considerably overpredicts the net formation rate of both molecular nitrogen and atomic oxygen outside the peak-temperature location. Whereas $\dot{w}_{N_2}^{mf}$ predicts positive production of N_2 beyond $y^* \simeq 20$, the actual mean production remains negative, corresponding to net depletion of N_2 throughout the entire boundary layer outside the viscous sublayer. Meanwhile, for atomic oxygen, the departures of $\dot{w}_O^{mf}$ from $\overline{\dot{w}}_O$ indicate that turbulence-induced thermodynamic fluctuations serve to both reduce the peak production of atomic oxygen by approximately 30 % and shift the location of maximum reactivity inward from $y^* \simeq 25$ to $y^* \simeq 16$. In the case of molecular oxygen and atomic nitrogen, in contrast, the mean-field approximation significantly overestimates the rate at which these species are depleted in the logarithmic layer of the boundary layer. In particular for atomic nitrogen, whereas the actual mean chemical production rate becomes essentially inactive beyond $y^* \simeq 100$, the mean-field approximation instead predicts considerable net depletion between $y^* \simeq 15$ and $y^* \simeq 1400$.

In order to assess the relative significance of specific thermodynamic fluctuations to this modulation of the mean chemical production rates, the auxiliary chemical reaction variables are required as

$$\overline{\mathcal{W}}_i^{\rho_j} = \int_{\mathbb{R}^{N_s+1}} \mathrm{d}\mathcal{V}\, \dot{w}_i(\{\rho_j\}, T)\delta\left(T - \widetilde{T}\right)\mathcal{P}(\{\rho_j\}), \tag{4.3}$$

and

$$\overline{\mathcal{W}}_i^{\theta} = \int_{\mathbb{R}^{N_s+1}} \mathrm{d}\mathcal{V}\, \dot{w}_i(\{\rho_j\}, T)\mathcal{P}(T)\prod_{\kappa=1}^{N_s}\delta\left(\rho_\kappa - \overline{\rho}_\kappa\right), \tag{4.4}$$

which correspond to the expected chemical production rates absent partial-density and temperature fluctuations, respectively. Numerical evaluation of the integrals in (4.1), (4.3) and (4.4), as well as all other auxiliary production-rate or reaction-rate variables to be introduced in this manuscript, are evaluated with a Monte Carlo method, utilising approximately 70 000 temporal samples of the fluctuations at $\hat{x} = 915$, $Re_{\delta_2} \simeq 2900$ over the course of 6.2 eddy turnovers. On the basis of the significant departures of both $\overline{\mathcal{W}}_i^{\theta}$ and $\overline{\mathcal{W}}_i^{\rho_j}$ from the mean chemical production rates, as reflected in figure 9, it is apparent that both thermal and compositional fluctuations give rise to the turbulence–chemistry interaction observed in the boundary layer. Particularly for the oxygenic species, neglecting partial-density fluctuations, as in the estimate given by $\overline{\mathcal{W}}_i^{\theta}$, proves a worse approximation of the mean chemical production rates than $\dot{w}_i^{mf}$ itself outside the peak-temperature location. In order to more precisely isolate the effects of specific thermodynamic-state

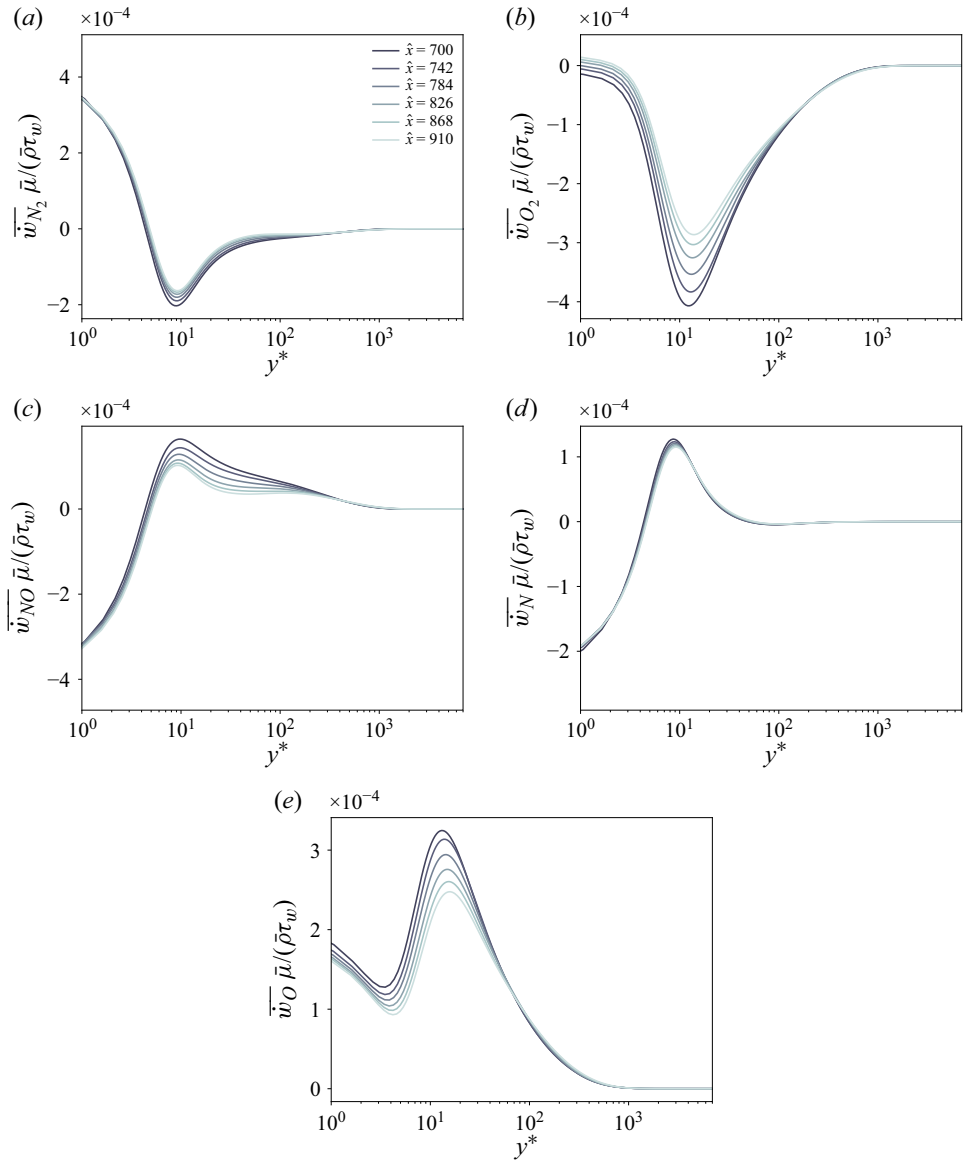

Figure 8. Reynolds-averaged net chemical production for (*a*) molecular nitrogen, (*b*) molecular oxygen, (*c*) nitric oxide, (*d*) atomic nitrogen and (*e*) atomic oxygen.

fluctuations, the Reynolds-averaged chemical production rates are decomposed as

$$\overline{\dot{w}}_i = \dot{w}_i^{mf} + \overline{\mathcal{I}}^{\rho_j}_{\mathcal{W}_i} + \overline{\mathcal{I}}^{\theta}_{\mathcal{W}_i} + \overline{\mathcal{I}}^{\rho_j,\theta}_{\mathcal{W}_i}, \tag{4.5}$$

where $\overline{\mathcal{I}}^{\rho_j}_{\mathcal{W}_i}$, $\overline{\mathcal{I}}^{\theta}_{\mathcal{W}_i}$ correspond to the distortion of mean chemical production rates arising solely from partial-density and thermal fluctuations, respectively. In contrast, the final term in the decomposition, $\overline{\mathcal{I}}^{\rho_j,\theta}_{\mathcal{W}_i}$, represents the net effect of the statistical co-moments of temperature and partial-density fluctuations on the mean chemical production rates. Utilising the auxiliary production variables introduced above, the first two terms in the

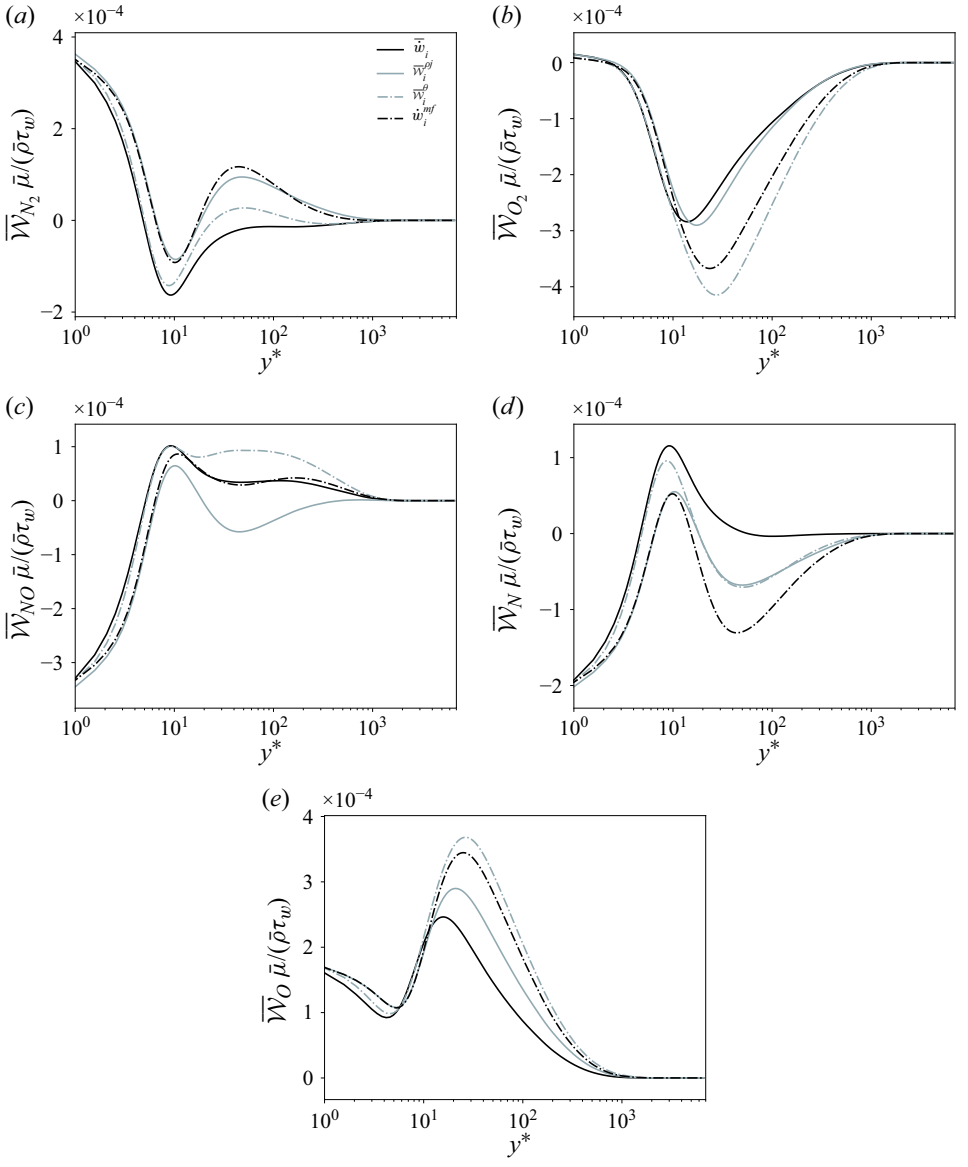

Figure 9. Reynolds-averaged chemical production variables for (*a*) molecular nitrogen, (*b*) molecular oxygen, (*c*) nitric oxide, (*d*) atomic nitrogen and (*e*) atomic oxygen.

decomposition can be directly evaluated as

$$\overline{\mathcal{I}}_{\mathcal{W}_i}^{\rho_j} = \overline{\mathcal{W}}^{\rho_j} - \dot{w}_i^{mf}, \tag{4.6}$$

$$\overline{\mathcal{I}}_{\mathcal{W}_i}^{\theta} = \overline{\mathcal{W}}_i^{\theta} - \dot{w}_i^{mf}, \tag{4.7}$$

while the final interaction term immediately follows as

$$\overline{\mathcal{I}}_{\mathcal{W}_i}^{\rho_j,\theta} = \overline{\dot{w}}_i + \dot{w}_i^{mf} - \overline{\mathcal{W}}_i^{\theta} - \overline{\mathcal{W}}_i^{\rho_j}, \tag{4.8}$$

where the summation of (4.6) through (4.8) recovers by construction the overall effect of turbulence–chemistry interaction on the production rates, $\overline{\dot{w}}_i - \dot{w}_i^{mf}$. As reflected

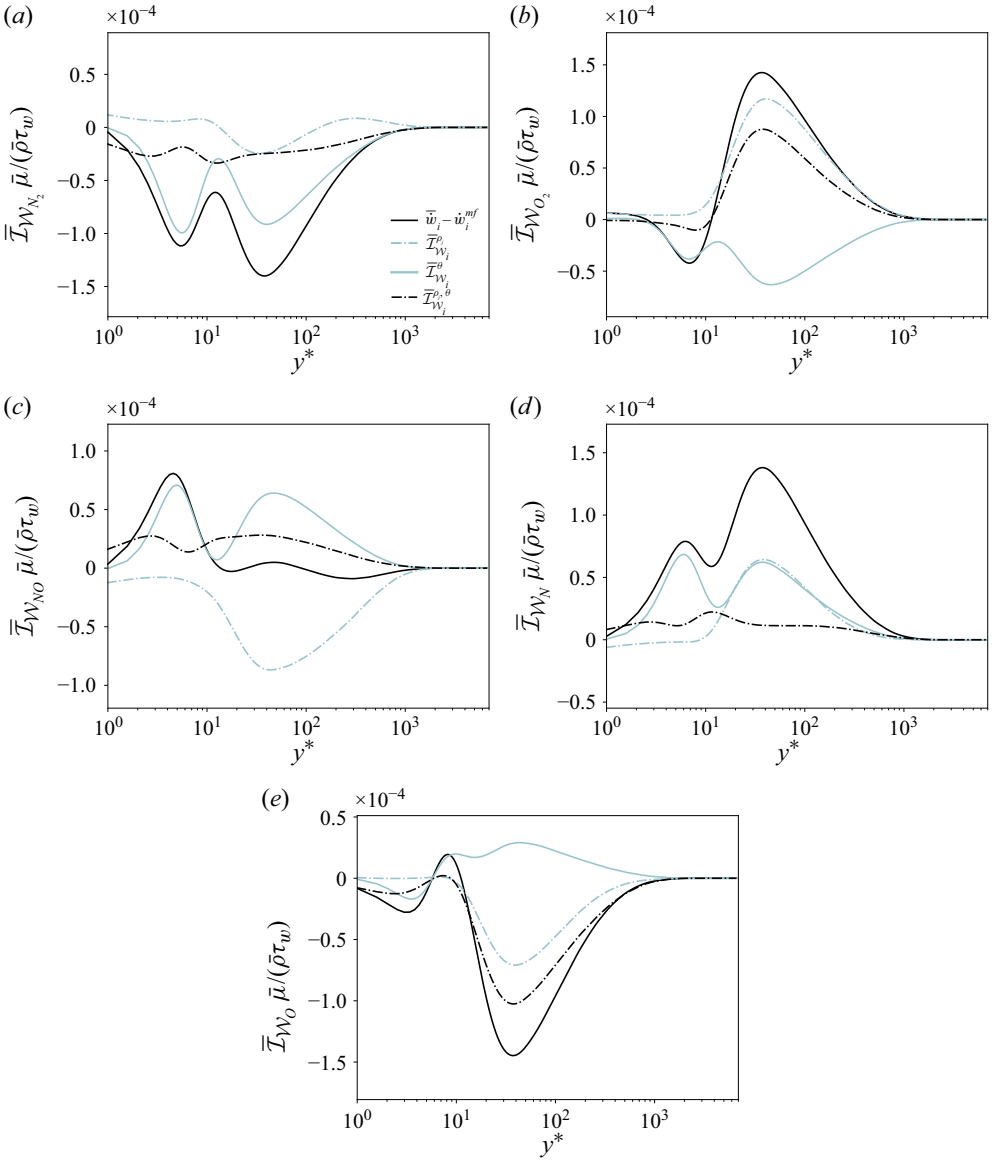

Figure 10. Reynolds-averaged thermodynamic decomposition of turbulence–chemistry interaction for net chemical production rates, corresponding to (*a*) molecular nitrogen, (*b*) molecular oxygen, (*c*) nitric oxide, (*d*) atomic nitrogen and (*e*) atomic oxygen.

in figure 10, all contributions to the turbulence–chemistry interaction decomposition generally prove consequential for the net chemical production rate of each species, with the maximum absolute distortion of the production rates attained in the vicinity of $y^* \simeq 40$ for all species apart from nitric oxide, with its corresponding production rate most increased by temperature fluctuations in the viscous sublayer. Indeed, while the contribution of temperature fluctuations alone to turbulence–chemistry interaction, as represented by $\overline{\mathcal{I}}^{\theta}_{\mathcal{W}_i}$, accounts for much of the overall distortion of the production rates for all species in the near-wall region bounded by the peak-temperature location, the effects of species

mixing becomes significant outside $y^* \simeq 10$. For the chemical production of molecular and atomic oxygen, in particular, the impact of partial-density fluctuations combines constructively with the joint effect of partial-density/temperature fluctuations to produce significant turbulence–chemistry interactions outside the temperature peak, decreasing the consumption rate of the molecular species and correspondingly inhibiting the production of atomic oxygen. Likewise, for atomic nitrogen, the separate effects of temperature and partial-density fluctuations, both serve to increase the chemical production rate beyond $y^* \simeq 10$, giving rise to a global maximum in the turbulence–chemistry interaction effect at the edge of the buffer layer and essentially eliminating consumption of atomic nitrogen outside the temperature peak. Correspondingly, the positive production of molecular nitrogen is largely suppressed by turbulence–chemistry interaction in the buffer and logarithmic layers owing primarily to temperature fluctuations. Finally, for the production of nitric oxide outside the buffer layer, the effect of partial-density fluctuations alone proves more consequential than the thermal fluctuations with respect to the mean distortion of the chemical production rate. As implied by the relatively close alignment of $\dot{w}_{NO}^{mf}$ and $\overline{\dot{w}}_{NO}$ in figure 9(*c*), however, the modulation of the nitric-oxide production rate by partial-density fluctuations alone is cancelled by the combined effect of thermal fluctuations and non-zero temperature/partial-density co-moments. As such, the modulation of the net nitric-oxide production rate proves most significant within peak-temperature location, where near-wall thermal fluctuations serve to amplify its net production.

4.4. *Modulation of chemical reaction rates by thermodynamic fluctuations*

To characterise the effect of thermodynamic fluctuations on specific reactions, an analogous decomposition to (4.5) can be invoked for the chemical reaction rates themselves, namely

$$\overline{\mathcal{R}}_i = \mathcal{R}_i^{mf} + \overline{\mathcal{I}}_{\mathcal{R}_i}^{\rho_j} + \overline{\mathcal{I}}_{\mathcal{R}_i}^{\theta} + \overline{\mathcal{I}}_{\mathcal{R}_i}^{\rho_j,\theta}, \tag{4.9}$$

where $\overline{\mathcal{R}}_i$ denotes the Reynolds-averaged reaction rate and $\mathcal{R}_i^{mf} = \mathcal{R}_i(\{\overline{\rho}_j\}, \widetilde{T})$ corresponds to its mean-field approximation based on the averaged thermodynamic fields. The corresponding expressions for the turbulence–chemistry interaction terms in (4.9), as well as auxiliary reaction-rate variables, can be evaluated precisely as in (4.3) through (4.8), merely exchanging $\mathcal{W}_i$ with $\mathcal{R}_i$. The averaged auxiliary reaction-rate variables are plotted as a function of the semi-local wall-normal coordinate in figure 11, confirming that the mean-field approximation of each reaction rate departs significantly from the Reynolds average itself, with the exception of the dissociation/recombination of molecular oxygen, which exhibits only modest net turbulence/chemistry interaction. The location of maximum distortion of the mean reaction rates by turbulent fluctuations naturally depends on the parameters of the reaction itself: whereas the shuffle reactions in the Zel'dovich mechanism, characterised by relatively lower activation energies, are primarily affected in the buffer and logarithmic layers, the dissociation/recombination processes naturally exhibit the most significant net turbulence–chemistry interaction near the peak-temperature location. In particular, for the Zel'dovich mechanism, the thermodynamic fluctuations serve to reduce the predominance of the reverse reaction, most significantly in the buffer layer. In light of the relative magnitudes of the turbulence–chemistry interaction terms for each reaction, it becomes apparent that the modulation of the net chemical production rates by turbulent fluctuations outside the peak-temperature location can largely be attributed to turbulence–chemistry interactions specific to the

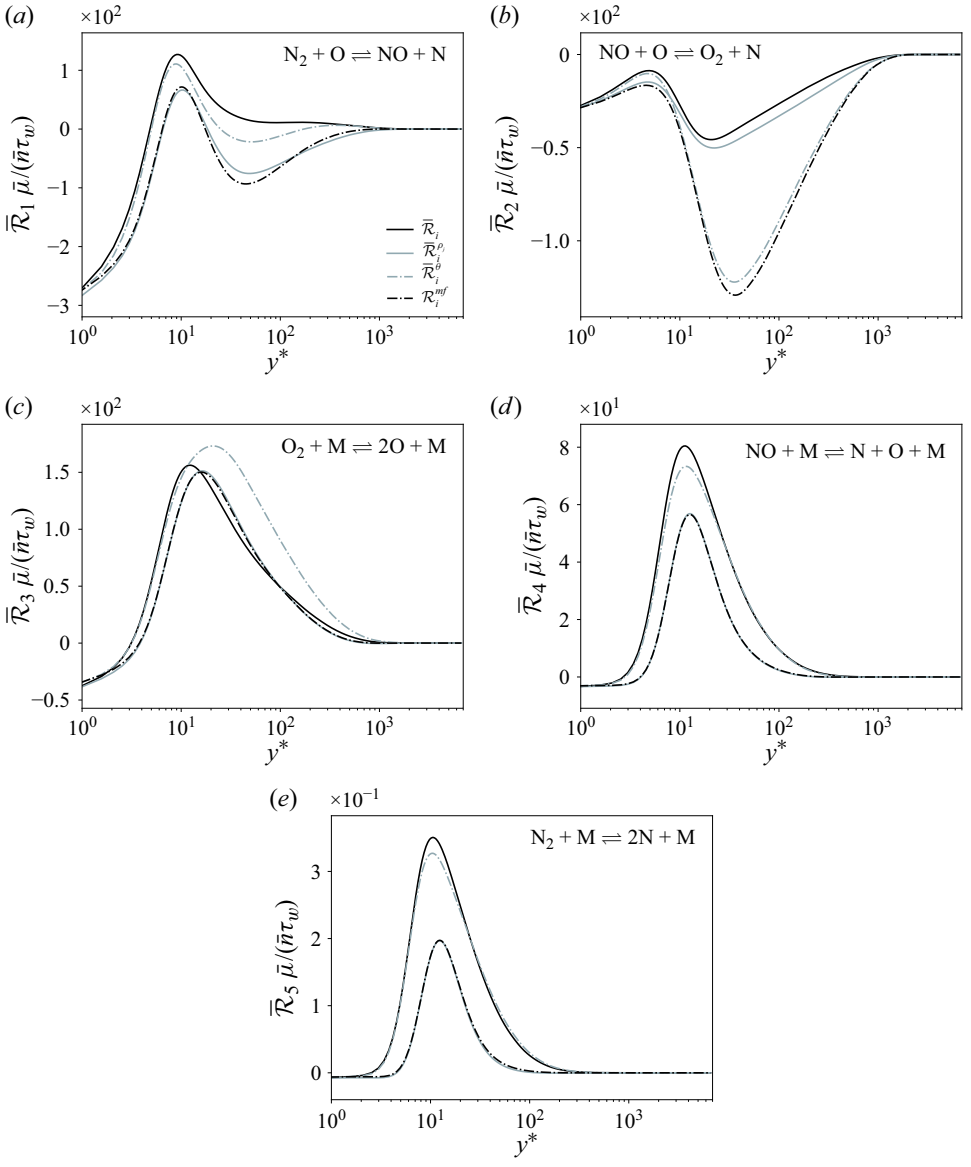

Figure 11. Reynolds-averaged chemical reaction-rate variables for (*a*,*b*) Zel'dovich exchange reactions, and dissociation/recombination of (*c*) molecular oxygen, (*d*) nitric oxide and (*e*) molecular nitrogen.

Zel'dovich shuffle reactions and not the dissociation/recombination processes. Instead, the mean dissociation rate of all molecular species is naturally maximised in the vicinity of the peak-temperature location, approximately aligned with the location of maximum turbulence–chemistry interaction for the dissociation of N_2 and O_2. Due to wall-cooling effects, a near-wall region characterised by net recombination of the atomic constituents ultimately emerges, the extent of which is contracted due to fluctuations. Whereas the mean-field approximation implies a recombination layer extending from the wall to $y^* \simeq 4$ for each molecular species, the actual recombination region based on the Reynolds-averaged reaction rates extends only to $y^* \simeq 3$. The close alignment between $\overline{\mathcal{R}}_i^{\theta}$ and $\overline{\mathcal{R}}_i$

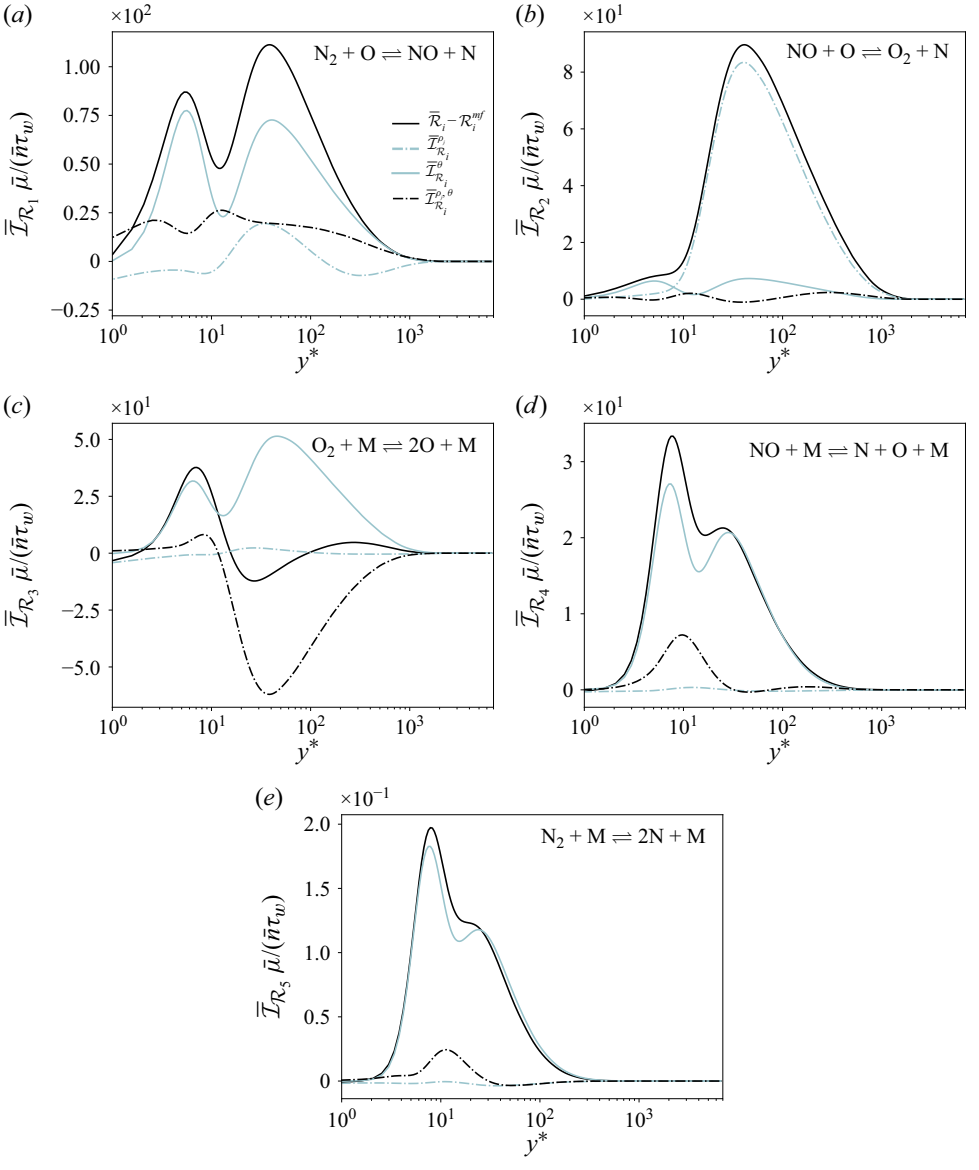

Figure 12. Reynolds-averaged thermodynamic decomposition of turbulence–chemistry interaction for chemical reaction rates, corresponding to (*a*,*b*) Zel'dovich exchange reactions, and dissociation/recombination of (*c*) molecular oxygen, (*d*) nitric oxide and (*e*) molecular nitrogen.

within the temperature peak confirms that the introduction of turbulence-induced thermal fluctuations alone accounts for the expansion of the dissociation layer centred at the temperature peak, thereby confining the recombination region closer to the non-catalytic surface.

As observed in the statistics of the auxiliary chemical production variables, the chemical reaction rates for both the Zel'dovich mechanism and the molecular dissociation/recombination processes are most significantly modulated by temperature fluctuations alone inside the peak-temperature location, although $\overline{I}^{\theta}_{\mathcal{R}_i}$ necessarily vanishes

at the wall itself due to isothermal wall condition. As reflected in figure 12, the near-wall temperature fluctuations increase the forward bias of each reaction, giving rise to local maxima in the turbulence–chemistry interactions between the edge of the viscous sublayer and the peak-temperature location. In particular, the turbulence–chemistry interaction observed for the first Zel'dovich reaction qualitatively parallels the turbulence–chemistry interaction observed in the chemical production of its reactant N_2, in that the distortion of the mean reaction rate is characterised by two local maxima adjacent to the temperature peak. While the inner maxima in the rate of (R1) is largely due to temperature fluctuations alone, the outer peak in turbulence–chemistry interaction is influenced more significantly by partial-density and joint partial-density/temperature fluctuations, increasing the generation rate of NO and N radicals. In contrast, the second Zel'dovich shuffle reaction proves far less sensitive to thermal fluctuations, although temperature fluctuations account for most of the forward biasing of the reaction rate within the peak-temperature location. Instead, the significant increase in the net forward rate of the reaction outside $y^* \simeq 10$ arises primarily due to partial-density fluctuations alone, ultimately contributing to heightened production rates for molecular oxygen and atomic nitrogen as observed in figure 9. For the dissociation/recombination of molecular oxygen, the global maximum in turbulence/chemistry interaction is located just within the peak-temperature location, corresponding to amplified dissociation due almost entirely to temperature fluctuations. For semi-local off-wall displacements exceeding $y^* \simeq 20$, however, the overall distortion of the mean O_2 dissociation/recombination rate proves quite limited. While turbulent fluctuations marginally decrease the effective dissociation rate between $y^* \simeq 20$ and $y^* \simeq 100$, temperature fluctuations alone give rise to an incremental augmentation in the net dissociation rate in the logarithmic layer of the boundary layer. This relatively negligible net turbulence–chemistry interaction, however, represents an approximate balance between the far more significant effects of temperature and joint partial-density/temperature fluctuations. That is, while the transport of temperature fluctuations alone from the peak-temperature location to the buffer and logarithmic layers serves to increase local dissociation rate significantly, the simultaneous transport of the pre-dissociated mixture from the inner part of the aerodynamic heating layer correspondingly displaces the necessary undissociated reactants, such that $\overline{\mathcal{I}}^{\theta}_{\mathcal{R}_i} \approx -\overline{\mathcal{I}}^{\rho_j,\theta}_{\mathcal{R}_i}$. For molecular nitrogen and nitric oxide dissociation/recombination, in contrast, the most significant contribution to the net turbulence–chemistry interaction remains $\overline{I}^{\theta}_{\mathcal{R}_i}$ throughout the boundary layer, owing to their relatively higher activation temperatures. To a far lesser extent, and localised near the peak-temperature location, the joint effect of temperature/partial-density fluctuations, as measured by $\overline{I}^{\rho_j,\theta}_{\mathcal{R}_i}$, does modestly alter the mean reaction rates for N_2 and NO. Deferred to Appendix D for the sake of brevity, the impact of partial-density fluctuations on the chemical reaction rates can be further decomposed in terms of each species, confirming that joint temperature/reactant-partial-density fluctuations, as well as temperature/radical-partial-density fluctuations, are the most significant contributions to $\overline{\mathcal{I}}^{\rho_j,\theta}_{\mathcal{R}_i}$ for the dissociation/recombination processes. In the particular case of molecular oxygen dissociation/recombination, joint ρ_{O_2}/temperature fluctuations almost fully comprise contributions to the overall turbulence–chemistry interaction captured by $\overline{I}^{\rho_j,\theta}_{\mathcal{R}_i}$.

4.5. *Impact of density fluctuations on turbulence/aerothermochemistry interactions*

To further separate the effect of overall density variation from compositional fluctuations on the mean reaction rates, the set of variables defining the thermodynamic state is now

chosen to be $\rho, Y_1, Y_2, \ldots, Y_{N_s-1}, T$. With this alternative choice of thermodynamic variables, the analogous decomposition to (4.9) is given by

$$\overline{\mathcal{R}}_i = \mathcal{R}_i^{mf} + \overline{\mathcal{I}}^{\rho}_{\mathcal{R}_i} + \overline{\mathcal{I}}^{Y_j}_{\mathcal{R}_i} + \overline{\mathcal{I}}^{\theta}_{\mathcal{R}_i} + \overline{\mathcal{I}}^{\rho,Y_j}_{\mathcal{R}_i} + \overline{\mathcal{I}}^{\rho,\theta}_{\mathcal{R}_i} + \overline{\mathcal{I}}^{Y_j,\theta}_{\mathcal{R}_i} + \overline{\mathcal{I}}^{\rho,Y_j,\theta}_{\mathcal{R}_i}, \tag{4.10}$$

where $\overline{\mathcal{I}}^{\rho}_{\mathcal{R}_i}$ and $\overline{\mathcal{I}}^{Y_j}_{\mathcal{R}_i}$ represent the mean effect of density and mass-fraction fluctuations on the ith reaction rate, respectively. In this formulation, the mean distortion of the chemical reaction rates due intrinsically to joint fluctuations in the thermodynamic state are given by $\overline{\mathcal{I}}^{\rho,Y_j}_{\mathcal{R}_i}$, $\overline{\mathcal{I}}^{\rho,\theta}_{\mathcal{R}_i}$, $\overline{\mathcal{I}}^{Y_j,\theta}_{\mathcal{R}_i}$ and $\overline{\mathcal{I}}^{\rho,Y_j,\theta}_{\mathcal{R}_i}$, with the comma-separated variables appearing in the superscript denoting the relevant fluctuating variables for each term in the decomposition. The effects of density and composition fluctuations on the mean reaction rates are quantified as

$$\overline{\mathcal{I}}^{\rho}_{\mathcal{R}_i} = \int_{\mathbb{R}^{N_s+1}} \mathrm{d}\mathcal{Y}\, \mathcal{R}_i(\{\rho Y_j\}, T)\mathcal{P}(\rho) \prod_{\kappa=1}^{N_s-1} \delta(Y_\kappa - \widetilde{Y}_\kappa)\delta(T - \widetilde{T}) - \mathcal{R}_i^{mf}, \tag{4.11}$$

and

$$\overline{\mathcal{I}}^{Y_j}_{\mathcal{R}_i} = \int_{\mathbb{R}^{N_s+1}} \mathrm{d}\mathcal{Y}\, \mathcal{R}_i(\{\rho Y_j\}, T)\delta(\rho - \overline{\rho})\mathcal{P}(\{Y_j\})\delta(T - \widetilde{T}) - \mathcal{R}_i^{mf}, \tag{4.12}$$

respectively, where $\mathrm{d}\mathcal{Y} = \mathrm{d}\rho\mathrm{d}T \prod_{\kappa=1}^{N_s-1} \mathrm{d}Y_\kappa$ is the differential volume element for the given set of thermodynamic variables. The joint interaction terms involving two thermodynamic quantities can likewise be evaluated as

$$\overline{\mathcal{I}}^{\rho,Y_j}_{\mathcal{R}_i} = \int_{\mathbb{R}^{N_s+1}} \mathrm{d}\mathcal{Y}\, \mathcal{R}_i(\{\rho Y_j\}, T)\mathcal{P}(\rho, \{Y_j\})\delta(T - \widetilde{T}) - \overline{\mathcal{I}}^{\rho}_{\mathcal{R}_i} - \overline{\mathcal{I}}^{Y_j}_{\mathcal{R}_i} - \mathcal{R}_i^{mf}, \tag{4.13}$$

$$\overline{\mathcal{I}}^{\rho,\theta}_{\mathcal{R}_i} = \int_{\mathbb{R}^{N_s+1}} \mathrm{d}\mathcal{Y}\, \mathcal{R}_i(\{\rho Y_j\}, T)\mathcal{P}(\rho, T) \prod_{\kappa=1}^{N_s-1} \delta(Y_\kappa - \widetilde{Y}_\kappa) - \overline{\mathcal{I}}^{\rho}_{\mathcal{R}_i} - \overline{\mathcal{I}}^{\theta}_{\mathcal{R}_i} - \mathcal{R}_i^{mf}, \tag{4.14}$$

$$\overline{\mathcal{I}}^{Y_j,\theta}_{\mathcal{R}_i} = \int_{\mathbb{R}^{N_s+1}} \mathrm{d}\mathcal{Y}\, \mathcal{R}_i(\{\rho Y_j\}, T)\delta(\rho - \overline{\rho})\mathcal{P}(\{Y_j\}, T) - \overline{\mathcal{I}}^{Y_j}_{\mathcal{R}_i} - \overline{\mathcal{I}}^{\theta}_{\mathcal{R}_i} - \mathcal{R}_i^{mf}, \tag{4.15}$$

while the contribution to turbulence/chemistry interaction associated with fluctuations in all variables, i.e. $\overline{\mathcal{I}}^{\rho,Y_j,\theta}_{\mathcal{R}_i}$, then follows immediately from (4.10). Each term in this more fine-grained decomposition is represented as a function of the semi-local coordinate in figure 13, disambiguating the relative impact of density and compositional variations. Direct effects from density fluctuations alone, as measured by $\overline{\mathcal{I}}^{\rho}_{\mathcal{R}_i}$, are found to be relatively unimportant, apart from the recombination layer where $\overline{\mathcal{I}}^{\rho}_{\mathcal{R}_i}$ accounts for additional reverse-reaction activity, representing fractionally significant contributions to the overall turbulence–chemistry interaction for the first Zel'dovich shuffle reaction and oxygen recombination in this very near-wall region. Apart from this relative importance in the recombination layer where the net turbulence–chemistry interaction itself remains quite modest, however, the direct effect of density fluctuations proves largely negligible for all reactions in the buffer and logarithmic layers. In contrast, the direct effect of compositional fluctuations as measured by $\overline{\mathcal{I}}^{Y_j}_{\mathcal{R}_i}$ represents a major contribution to the net turbulence–chemistry interaction for both shuffle reactions, and to a lesser extent, the dissociation of molecular oxygen. In particular, for the second Zel'dovich reaction, outside the peak-temperature location, the compositional fluctuations alone are primarily

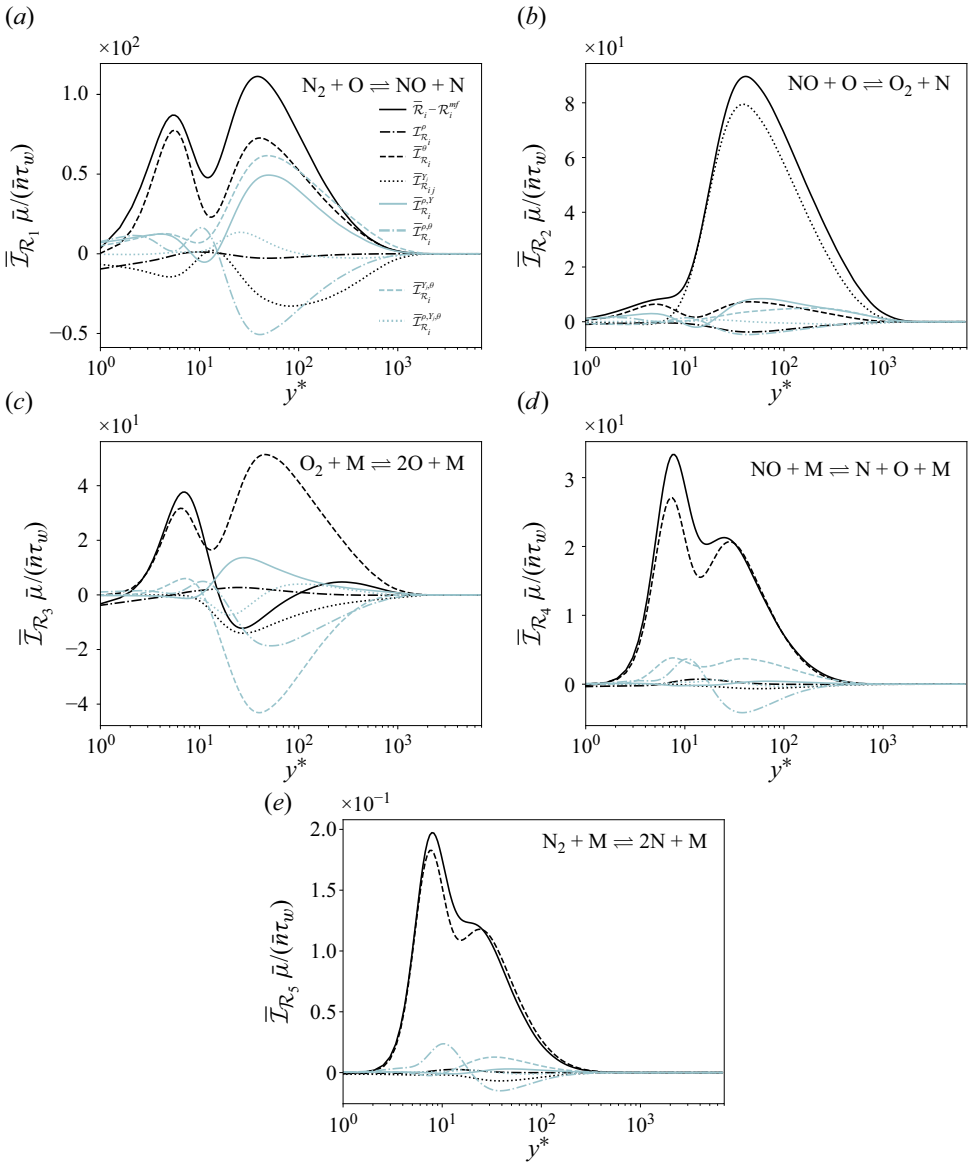

Figure 13. Reynolds-averaged decomposition, with the thermodynamic state as defined by density, temperature and composition, for the impact of turbulence–chemistry interaction on chemical reaction rates. The panels correspond to (*a*,*b*) the Zel'dovich exchange reactions, and dissociation/recombination of (*c*) molecular oxygen, (*d*) nitric oxide and (*e*) molecular nitrogen, respectively.

responsible for the overall distortion of the mean reaction rates. Hence the significant reduction in the net backwards-direction reactivity previously associated with the partial-density fluctuations can be more precisely attributed to mass-fraction fluctuations. For (R1) and (R3), compositional fluctuations favour the backward reaction rates outside the peak-temperature location, although separately attaining their maximum absolute values in the logarithmic and buffer layers, respectively.

In the case of the first Zel'dovich reaction, all of the two-variable joint interaction terms between the thermodynamic variables prove significant, with the joint effects of

compositional/temperature and composition/density fluctuations effectively increasing the net positivity of the reaction rate, while the net impact from joint density/temperature fluctuations is to correspondingly increase the backward reaction activity. For oxygen dissociation, however, the effect of joint fluctuations in composition and temperature emerges as the most significant, effectively negating the impact of temperature fluctuations. Hence, the effective suppression of the forward reaction rate by $\overline{\mathcal{I}}^{\rho_j,\theta}_{\mathcal{R}_3}$ observed previously can be largely attributed to the coupling of mass-fraction/temperature fluctuations consistent with the simultaneous transport of high-temperature fluid, depleted of molecular oxygen, outwards from the aerodynamic heating layer.

4.6. *Intrinsic-compressibility effects on finite-rate chemical processes*

The density variations present in the boundary layer arise from a combination of pressure, entropic and compositional perturbations (Kovasznay 1953; Griffond 2005; Livescu 2020). With Morkovin's hypothesis relying on the relative insignificance of intrinsic-compressibility effects and hence pressure fluctuations (Morkovin 1962; Lele 1994), its validity for mean reaction-rate statistics can be assessed in part by evaluating the departure of the isobaric reaction rates

$$\overline{\mathcal{R}}_i^p = \int_{\mathbb{R}^{N_s+1}} \mathrm{d}\mathcal{Y}\, \mathcal{R}_i(\{\rho Y_j\}, T)\delta\left(\rho - \frac{\overline{P}\mathcal{M}}{R^0 T}\right)\mathcal{P}(\{Y_j\}, T), \tag{4.16}$$

for which the density fluctuations are modelled as entirely entropic, from the corresponding Reynolds-averaged counterparts. Alternatively, in approximating the density fluctuations as arising from isentropic pressure waves (Ristorcelli & Blaisdell 1997; Griffond 2005; Donzis & Jagannathan 2013), propagative or otherwise, the implied isentropic reaction rates are given by

$$\overline{\mathcal{R}}_i^s = \int_{\mathbb{R}^{N_s+1}} \mathrm{d}\mathcal{Y}\, \mathcal{R}_i(\{\rho Y_j\}, T)\delta\left(\rho - \frac{\overline{P}\mathcal{M}}{R^0 T}\left(1 + \frac{(\gamma-1)T'}{\gamma\overline{T}}\right)\right)\mathcal{P}(\{Y_j\}, T). \tag{4.17}$$

Finally, to characterise the impact of compositional fluctuations, while retaining both entropic and pressure disturbances, the mean isoconcentration reaction rates are defined as

$$\overline{\mathcal{R}}_i^c = \int_{\mathbb{R}^2} \mathrm{d}P\mathrm{d}T\, \mathcal{R}_i\left(\frac{P\mathcal{M}|_{\overline{Y}_j}}{R^0 T}\{\overline{Y}_j\}, T\right)\mathcal{P}(P, T), \tag{4.18}$$

where $\mathcal{M}|_{\overline{Y}_j}$ denotes the mixture's molar mass based on the Reynolds-averaged mass fractions. Given the presence of near-wall viscous transport and chemical reactions, the entropic, compositional and pressure waves, which evolve independently in the small-disturbance limit, couple in the turbulent boundary layer (Livescu 2020). Nevertheless, as reflected in figure 14, the isobaric approximation for the turbulent reaction rates exhibits close agreement with the corresponding Reynolds averages, particularly with respect to the Zel'dovich reactions. While pressure fluctuations in the buffer layer give rise to slight discrepancies between $\overline{\mathcal{R}}_i^p$ and $\overline{\mathcal{R}}_i$ near $y^* \simeq 10$, this difference effectively vanishes in both the viscous sublayer and logarithmic region. In contrast, the isentropic approximation, in implicitly correlating temperature fluctuations with compression of the flow, give rises to significant overprediction of the net dissociation rates, in a region extending from the viscous sublayer through the logarithmic layer. The isoconcentration reaction-rate variables likewise depart significantly from the Reynolds averages outside the viscous sublayer, for all reactions apart from nitrogen and nitric-oxide dissociation.

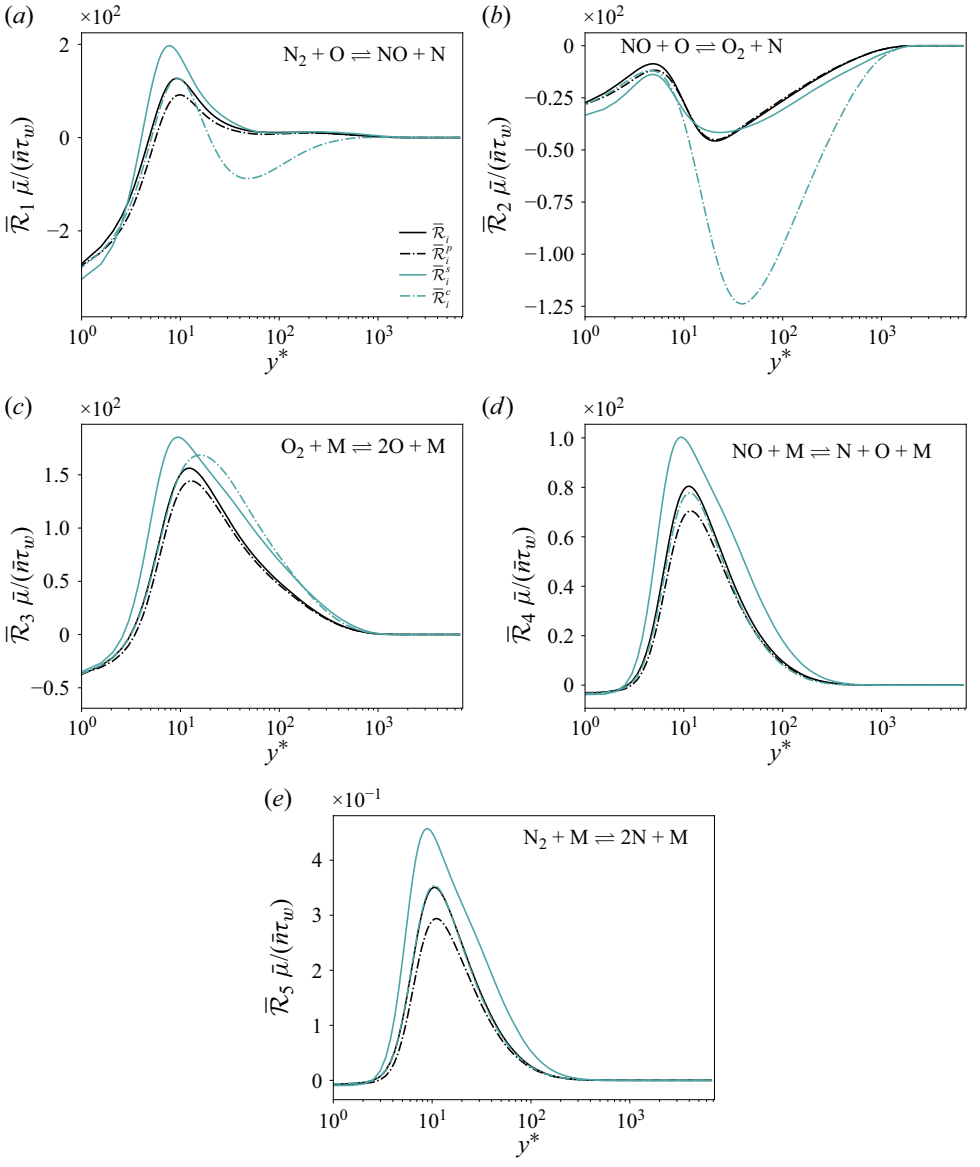

Figure 14. Reynolds-averaged chemical reaction rates juxtaposed with the mean auxiliary reaction-rate variables neglecting pressure, entropic and compositional fluctuations, for the (*a*,*b*) Zel'dovich mechanism, and dissociation/recombination of (*c*) molecular oxygen, (*d*) nitric oxide and (*e*) molecular nitrogen.

Following from the law of mass action, the isobaric, isentropic and isoconcentration chemical production rates are evaluated in terms of the auxiliary reaction-rate variables as $\overline{\mathcal{W}}_i^m = \mathcal{M}_i \sum_{j=R_1}^{R_5} (\nu''_{ij} - \nu'_{ij}) \overline{\mathcal{R}}_j^m$, where m represents the given mode neglected, i.e. $m \in p, s, c$. In terms of the net production rates of each species and owing to the behaviour observed in the individual chemical reactions, the pressure perturbations generally prove far less significant than the counterpart fluctuations in entropy and composition throughout virtually the entire boundary layer, as shown in figure 15. While this comparison of the Reynolds-averaged and auxiliary chemical-production variables implicitly neglects the

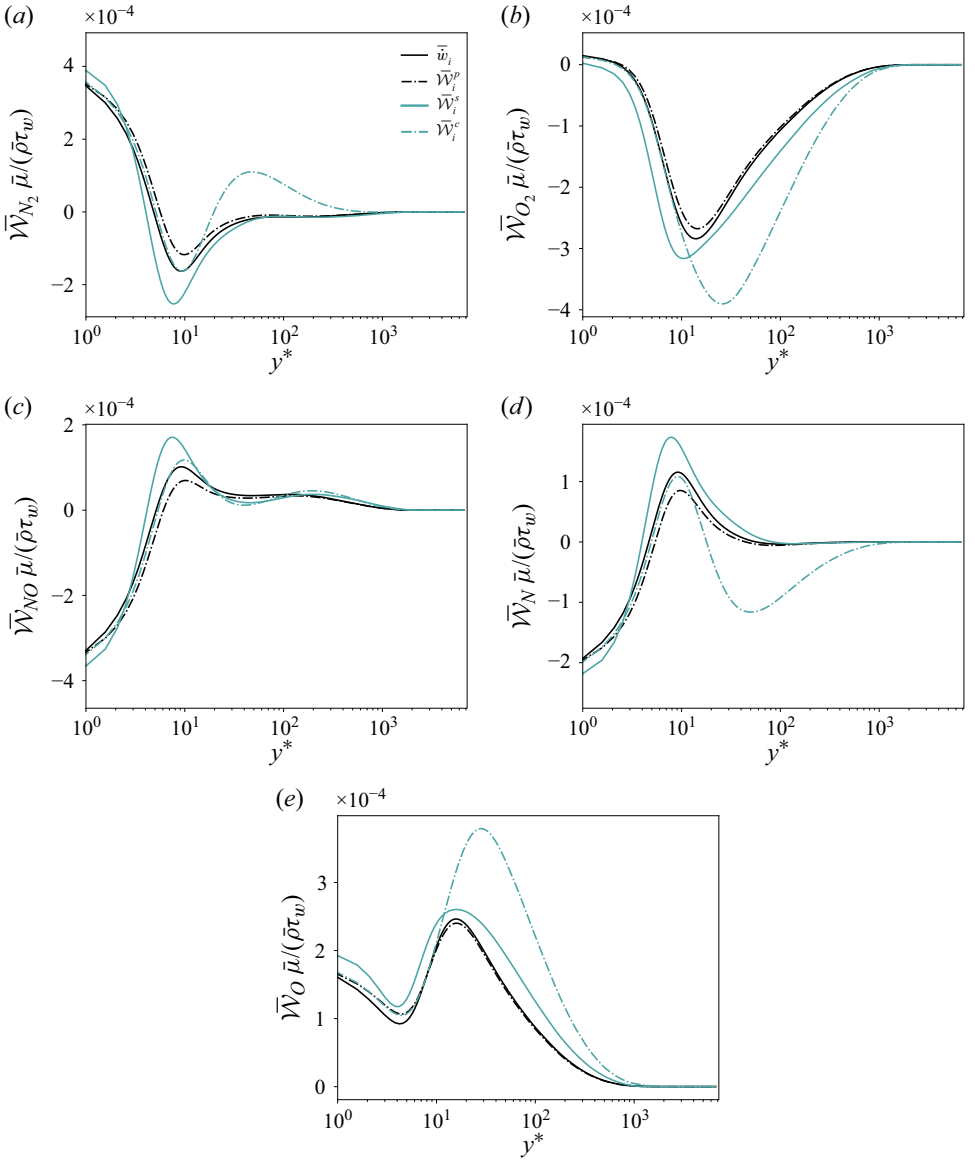

Figure 15. Reynolds-averaged chemical production rates juxtaposed with the mean auxiliary production-rate variables neglecting pressure, entropic and compositional fluctuations, for (*a*) molecular nitrogen, (*b*) molecular oxygen, (*c*) nitric oxide, (*d*) atomic nitrogen and (*e*) atomic oxygen.

impact of pressure fluctuations on establishing the turbulent base flow and corresponding thermodynamic fluctuations themselves, it nevertheless provides strong evidence for a consistent extension of Morkovin's hypothesis, namely, that turbulence–chemistry interaction in high-speed boundary layers arises primarily from a combination of entropic and compositional fluctuations, with pressure perturbations effecting only marginal impact within the buffer layer.

5. Conclusions

In order to characterise turbulence–aerothermochemistry interactions in high-Mach external flows, this manuscript presents numerical simulations and statistical analyses of a turbulent hypersonic boundary layer, overriding a non-catalytic surface at 3000 K. With the flow remaining in chemical non-equilibrium, numerical integration of the compressible, reacting Navier–Stokes equations is performed to enable a finite-rate evolution of the composition fields corresponding to N_2, O_2, NO, N and O. An auxiliary calculation, comprising Mach-25 flow over a 16-degree sharp-nosed wedge yields an inflow laminar boundary layer with an edge Mach number of 7 and an edge temperature of 2686 K. This laminar base flow is forced to transition in the primary computational domain with spatially localised transpiration comprised of two oscillatory modes. Following breakdown to turbulence, the boundary layer ultimately attains a friction Reynolds and Mach numbers of $Re_\tau \simeq 1200$ and $Ma_\tau \simeq 0.20$, respectively, with the turbulence integral time scales approximately equal to the characteristic chemical time scales. Chemical activity within the boundary layer, comprising dissociation/recombination reactions for each of the molecular species together with the Zel'dovich mechanism, gives rise to significant compositional variation throughout the boundary layer. Activated by a peak Favre-averaged temperature of approximately 5300 K, the chemical reactions produce considerable concentrations of radical species in the near-wall region. In particular, with the molecular oxygen almost entirely depleted within the peak-temperature location of $y^* \simeq 10$, the mean near-wall molar fraction of atomic oxygen reaches 0.27, whereas nitric oxide and atomic nitrogen attain their maximum concentrations in the buffer layer, with peak molar fractions of 0.06 and 0.01, respectively.

As a consequence of the near-unity turbulent Damköhler numbers, the chemical production rates within the aerodynamic heating layer are strongly modulated by turbulence-induced thermodynamic fluctuations, primarily through the exchange processes of the Zel'dovich reactions. In particular, the Reynolds-averaged production rates are shown to differ significantly from their respective mean-field approximations, for all species apart from nitric oxide. While the net depletion rates of both molecular oxygen and atomic nitrogen are severely overpredicted in the buffer and logarithmic layers based on the mean thermodynamic-state variables, the production rates of molecular nitrogen and atomic oxygen are correspondingly overestimated. In order to further characterise this turbulence–chemistry interaction, a computational approach for decomposing the impact of turbulence-induced thermodynamic fluctuations on chemical reactions and production rates is introduced. In general, both thermal and partial-density fluctuations, as well as the impact of their statistical co-moments, are shown to contribute significantly to the net chemical production rate of each species, with the maximum absolute distortion of the production rates attained outside the buffer layer. Within the near-wall region bounded by the peak-temperature location, however, the statistical decomposition reveals that temperature fluctuations alone account for much of the overall distortion of the production rates, with the effects of partial-density fluctuations generally becoming more significant outside $y^* \simeq 10$. Further aspects pertaining to the impact of turbulence-chemistry interaction on mean-flow predictions with reduced-order near-wall models are provided in Cogo *et al.* (2023*b*).

In terms of specific reactions, a comparison of the mean-field approximations and Reynolds averages reveals that while the shuffle reactions are primarily affected by thermodynamic fluctuations in the buffer and logarithmic layers, the dissociation/recombination processes in contrast exhibit the most significant distortion in the vicinity of the peak-temperature location, owing to their relatively higher

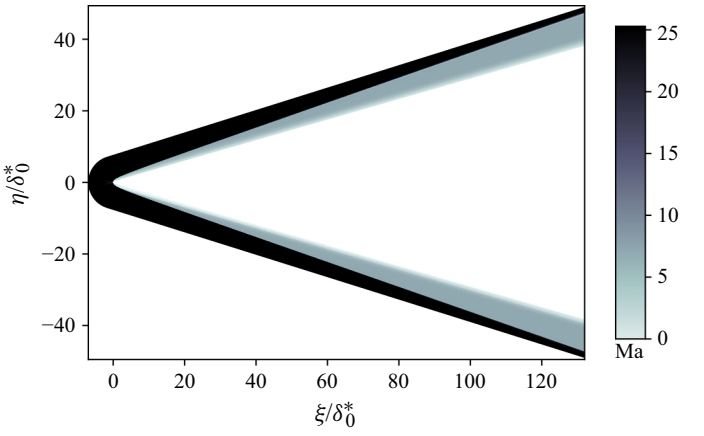

Figure 16. Mach-number contours from the numerical simulation of reacting hypersonic flow overriding a 16-degree wedge at an altitude of 25 km, from which the laminar boundary layer is extracted to provide the inflow boundary conditions.

activation energies. Moreover, inside the peak-temperature location, the chemical reaction rates for both the Zel'dovich mechanism and the molecular dissociation/recombination processes are most significantly modulated by temperature fluctuations alone. For dissociation/recombination processes in particular, these near-wall thermal fluctuations manifest in an augmentation of the molecular dissociation rate, thereby further confining the off-wall extent of the recombination layer. Compositional fluctuations are likewise shown to contribute significantly to the net turbulence–chemistry interaction for both shuffle reactions, and to a lesser extent, the dissociation of molecular oxygen. In the case of the second Zel'dovich reaction, the statistical decomposition introduced herein reveals that compositional fluctuations alone are primarily responsible for the overall distortion of its mean reaction rate and hence chemical production rates for all major species apart from molecular nitrogen. To isolate the impact of pressure perturbations on the mean chemical reaction rates, relative to the contributions from compositional and entropic modes, a final set of auxiliary reaction-rate variables is introduced, providing evidence for a consistent extension of Morkovin's hypothesis, that turbulence–chemistry interaction in high-Mach boundary layers primarily arises from a combination of entropic and compositional fluctuations, with pressure perturbations introducing only marginal reaction-rate distortions in the buffer layer.

Funding. This investigation was funded by the Advanced Simulation and Computing (ASC) program of the US Department of Energy's National Nuclear Security Administration (NNSA) via the PSAAP-III Center at Stanford, Grant No. DE-NA0002373. C.W. acknowledges support by the National Science Foundation Graduate Research Fellowship Program under Grant No. DGE-2146755.

Declaration of interests. The authors report no conflict of interest.

Appendix A. Incoming laminar hypersonic boundary layer

The laminar hypersonic boundary layer imposed at the inflow boundary of the Cartesian computational domain is extracted from an auxiliary calculation of the Mach-25 flow field around a 16-degree semi-angle hypersonic wedge, with a leading-edge radius of 0.2 mm. The free-stream pressure and temperature for the wedge simulation were taken to be 2549 Pa and 221 K, respectively, consistent with atmospheric conditions for hypersonic flight

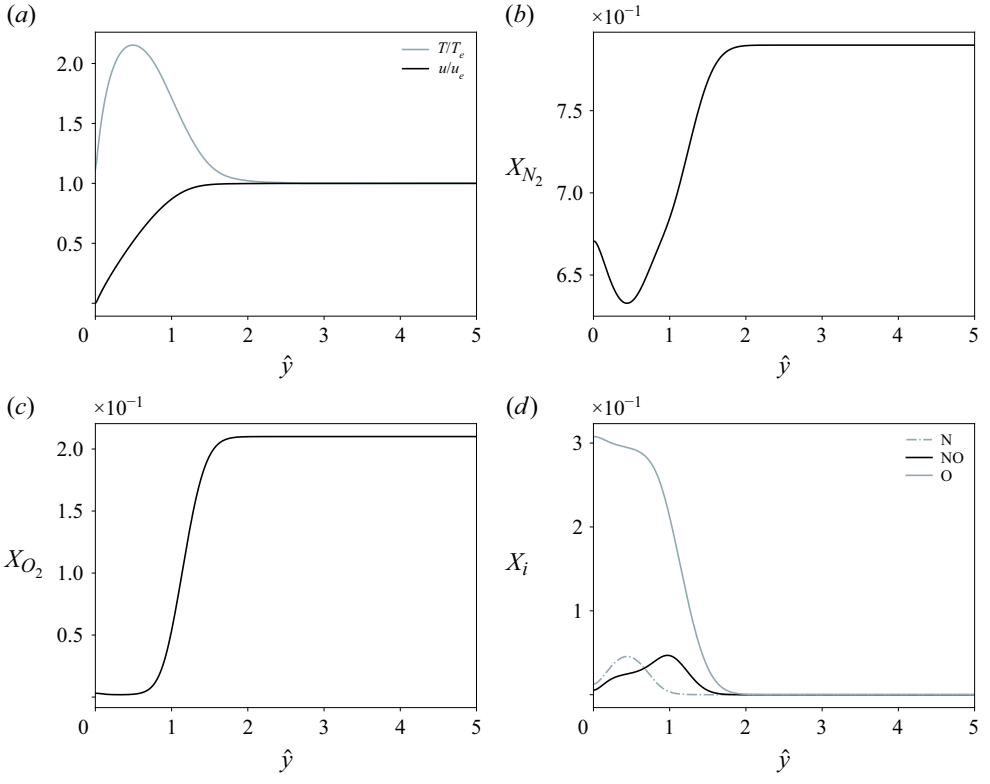

Figure 17. Laminar-boundary-layer profiles from reacting hypersonic wedge calculation utilised as inflow boundary conditions, corresponding to (*a*) temperature and streamwise velocity, (*b*) molecular-nitrogen molar fraction, (*c*) molecular-oxygen molar fraction and (*d*) molar fractions of radical species.

in the stratosphere at 25 km. This precursor simulation entailed direct integration of the conservation equations as formulated in Section 3 utilising a single-block curvilinear grid topology. Contours of the local Mach number from the numerical solution are presented in figure 16, in which the shock-induced heating and deceleration of the flow produces a shock layer with a nominal Mach number of 7 and pressure of 203.2 kPa. The laminar boundary-layer profiles are extracted approximately at 117 δ_0^* downstream of the leading edge, corresponding to a displacement-thickness Reynolds number of 6000. The temperature, molar fractions, and streamwise-velocity profiles for this boundary layer are provided in figure 17, for which the boundary-layer edge conditions have been artificially extended to exclude the oblique shock wave from the Cartesian turbulent boundary-layer simulation. These regularised boundary-layer profiles are then applied as the inflow boundary conditions for the turbulent boundary-layer calculation together with the shock-layer pressure.

Appendix B. Confirmation of turbulent state

As depicted in figure 18(*a*),the breakdown to turbulence in the boundary layer is evidenced by a rapid increase in and subsequent relaxation of the skin-friction and heat-flux coefficients near $\hat{x} \simeq 600$. Despite the addition of chemical reactivity and a relative increase in the edge Mach number, the present numerical simulation's skin-friction

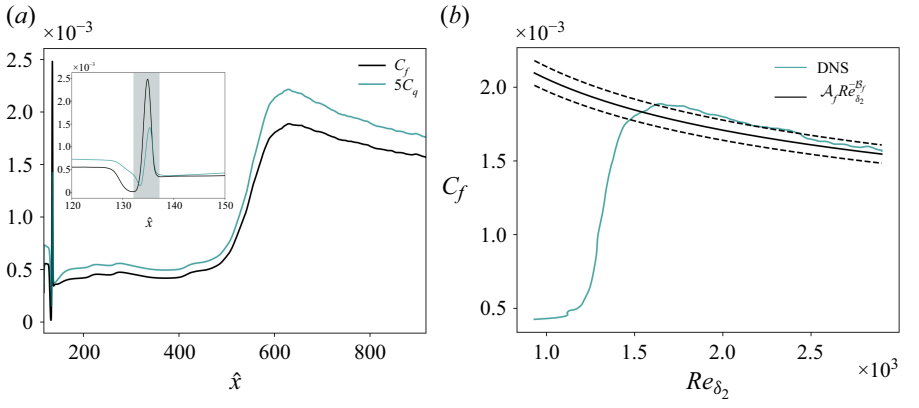

Figure 18. (*a*) Spatial evolution of the skin-friction and heat-flux coefficients through transition; inset depicts the same data localised near the forcing strip, denoted by the shaded region, (*b*) collapse of the skin-friction coefficient onto the correlation of Ceci *et al.* (2022), from which we utilise $\mathcal{A}_f = 0.0131$ and $\mathcal{B}_f = 0.268$. The dashed lines demarcate a $\pm 5\,\%$ interval relative to the nominal scaling.

coefficient collapses onto the correlation of Ceci *et al.* (2022) to within $\simeq 5\,\%$, as reflected in figure 18(*b*). The normalised power spectral density of velocity and concentration fluctuations in the fully turbulent regime at $\hat{x} = 915$ are provided in figure 19, which confirms that dominance of the forcing wavenumber does not persist through transition, and instead, the fluctuations exhibit the expected multi-scale behaviour. Likewise, no pileup in spectral density is observed at high wavenumbers, which in conjunction with the grid-sensitivity study presented in the following appendix, verifies the sufficiency of the numerical resolution. Finally, the corresponding two-point autocorrelation functions in figure 20 confirm that the velocity and molar-fraction fluctuations exhibit spatial decorrelation within separation distances less than 20 % of the spanwise extent.

Appendix C. Verification of grid convergence

In order to confirm the insensitivity of the relevant direct numerical simulation statistics to grid refinement, a secondary calculation of the Mach-7 reacting hypersonic boundary layer has been performed, discretised with approximately 1.5 times fewer points in each direction, yielding a total of 7920, 310 and 788 points across the streamwise, spanwise and wall-normal directions, respectively. In order to maintain the first off-wall grid point's location under coarsening, the hyperbolic-sine stretching factor in the wall-normal direction has been increased from 5.0 to 5.5 for the grid-convergence study. The transformed mean-flow streamwise velocity and Reynolds-stress components, as well as the Reynolds-averaged partial densities and chemical production rates, are provided in figure 21 for the coarse calculation. The very close alignment of its statistics with those of the fine grid confirms the grid insensitivity of the numerical solution results analysed in § 2 of this manuscript.

Appendix D. Species-specific decomposition of reaction-rate modulation by partial-density fluctuations

In order to isolate species-specific effects, further decomposition of the turbulence–chemistry interaction terms involving partial-density fluctuations, i.e. $\overline{\mathcal{I}}^{\rho_j}_{\mathcal{R}_i}$ and $\overline{\mathcal{I}}^{\rho_j,\theta}_{\mathcal{R}_i}$, yields

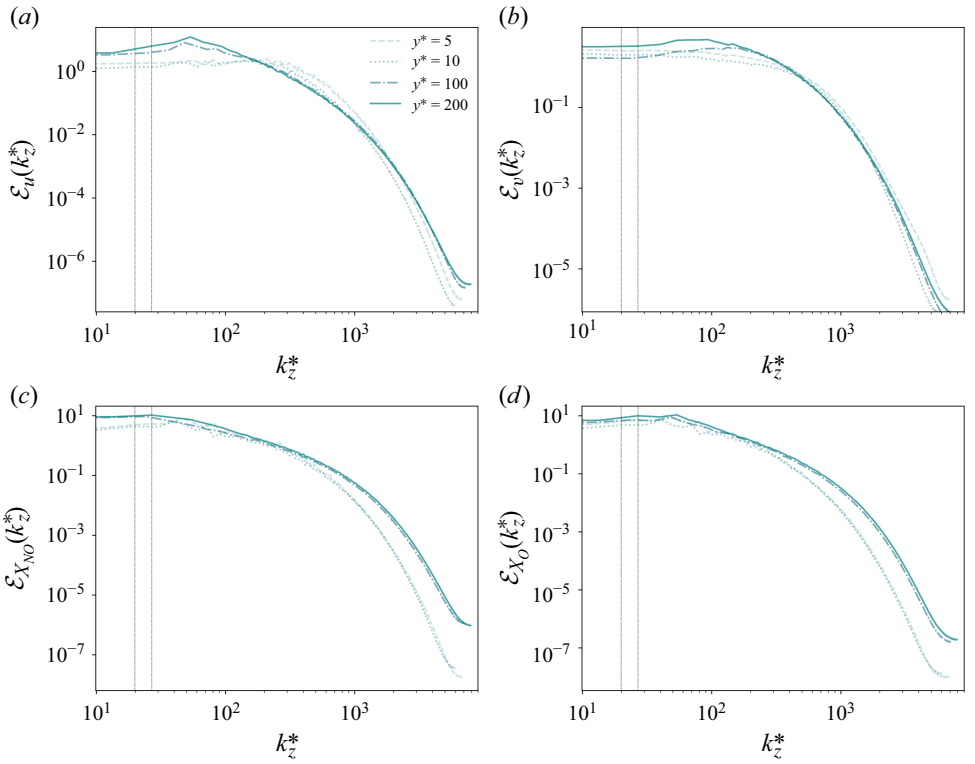

Figure 19. Normalised spanwise spectra for (*a*) streamwise velocity, (*b*) wall-normal velocity, (*c*) X_{NO} and (*d*) X_O fluctuations at $Re_{\delta_2} \simeq 2900$. Normalisation of the power spectral density is performed with the semi-local length scale and the total variance given by $\int \mathrm{d}k_z^* \mathcal{E}_\phi(k_z^*)$. The range of k_z^* associated with the numerical tripping in the laminar boundary layer is indicated by the dashed vertical lines.

a finer-grained decomposition

$$\overline{\mathcal{R}}_i = \mathcal{R}_i^{mf} + \overline{\mathcal{I}}_{\mathcal{R}_i}^{\theta} + \sum_{\alpha=1}^{N_s} \left(\overline{\mathcal{I}}_{\mathcal{R}_i}^{\rho_\alpha} + \overline{\mathcal{I}}_{\mathcal{R}_i}^{\rho_\alpha,\theta} \right) + \sum_{\alpha=1}^{N_s} \sum_{\gamma=\alpha+1}^{N_s} \overline{\mathcal{I}}_{\mathcal{R}_i}^{\rho_\alpha,\rho_\gamma} + \overline{\epsilon}_{\mathcal{R}_i}^{\rho_j} + \overline{\epsilon}_{\mathcal{R}_i}^{\rho_j,\theta}, \tag{D1}$$

where $\overline{\mathcal{I}}_{\mathcal{R}_i}^{\rho_\alpha}$, $\overline{\mathcal{I}}_{\mathcal{R}_i}^{\rho_\alpha,\theta}$ and $\overline{\mathcal{I}}_{\mathcal{R}_i}^{\rho_\alpha,\rho_\gamma}$ correspond to the mean distortion of the ith reaction rate arising from fluctuations in the partial density of species α alone, from fluctuations in both temperature and species-α partial density, and from fluctuations in the partial densities of species α and γ, respectively. The final two terms appearing in the decomposition, $\overline{\epsilon}_{\mathcal{R}_i}^{\rho_j}$, and $\overline{\epsilon}_{\mathcal{R}_i}^{\rho_j,\theta}$, capture the modulation of the mean chemical reaction rates stemming from fluctuations in the partial densities of three species, and from fluctuations in the partial densities of at least two species and temperature, respectively. These measures of turbulence–chemistry interaction can be expressed can in terms of the probability density of the thermodynamic fluctuations as

$$\overline{\mathcal{I}}_{\mathcal{R}_i}^{\rho_\alpha} = \int_{\mathbb{R}^{N_s+1}} \mathrm{d}\mathcal{V}\, \mathcal{R}_i(\{\rho_j\}, T)\delta(T - \widetilde{T})\mathcal{P}(\rho_\alpha) \prod_{\substack{\kappa=1,\\ \kappa\neq\alpha}}^{N_s} \delta(\rho_\kappa - \overline{\rho}_\kappa) - \mathcal{R}_i^{mf}, \tag{D2}$$

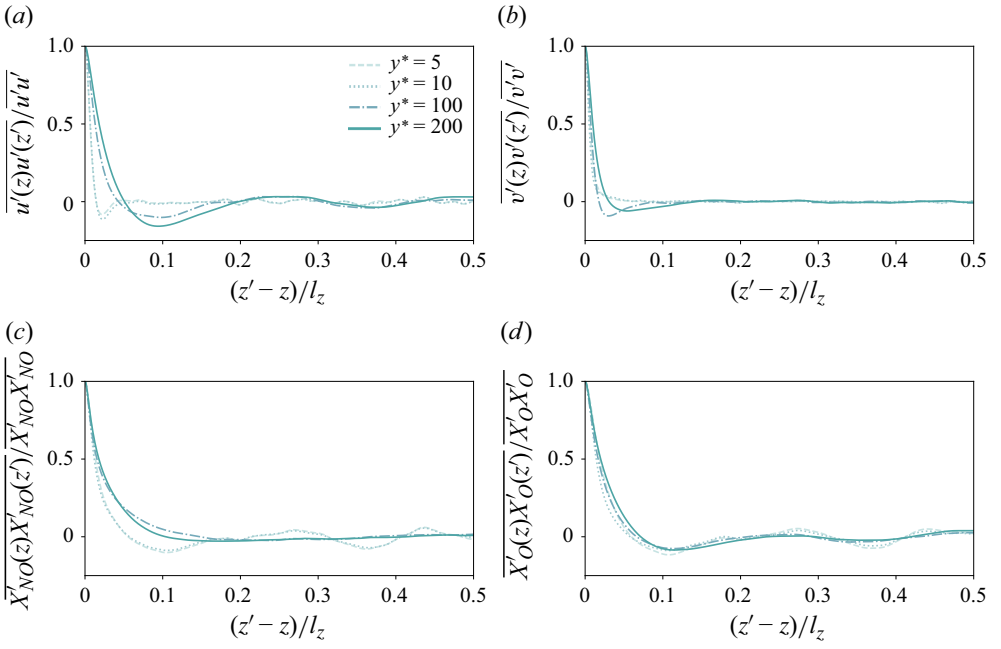

Figure 20. Two-point autocorrelation functions for (*a*) streamwise velocity, (*b*) wall-normal velocity, (*c*) X_{NO} and (*d*) X_O fluctuations as a function of the separation distance, $z - z'$, normalised by the total spanwise domain extent l_z.

$$\overline{\mathcal{I}}^{\rho_\alpha,\rho_\gamma}_{\mathcal{R}_i} = \int_{\mathbb{R}^{N_s+1}} \mathrm{d}\mathcal{V}\, \mathcal{R}_i(\{\rho_j\}, T)\delta(T-\widetilde{T})\mathcal{P}(\rho_\alpha, \rho_\gamma) \prod_{\substack{\kappa=1,\\ \kappa\neq\alpha,\gamma}}^{N_s} \delta(\rho_\kappa - \overline{\rho}_\kappa) - \overline{\mathcal{I}}^{\rho_\alpha}_{\mathcal{R}_i} - \overline{\mathcal{I}}^{\rho_\gamma}_{\mathcal{R}_i} - \mathcal{R}^{mf}_i, \tag{D3}$$

$$\overline{\epsilon}^{\rho_j}_{\mathcal{R}_i} = \overline{\mathcal{I}}^{\rho_j}_{\mathcal{R}_i} - \sum_{\alpha=1}^{N_s} \overline{\mathcal{I}}^{\rho_\alpha}_{\mathcal{R}_i} - \sum_{\alpha=1}^{N_s}\sum_{\gamma=\alpha+1}^{N_s} \overline{\mathcal{I}}^{\rho_\alpha,\rho_\gamma}_{\mathcal{R}_i}, \tag{D4}$$

where, given the bimolecularity of the Zel'dovich mechanism, $\overline{\epsilon}^{\rho_j}_{\mathcal{R}_i}$ is precisely zero for the nitric-oxide exchange reactions. With the impact of partial-density fluctuations shown to be most significant for the exchange reactions, the further decomposed reaction-rate distortion due to partial-density fluctuations is presented in figure 22 for the Zel'dovich mechanism, as a function of the semi-local wall-normal distance. For the first of the shuffle reactions, while joint fluctuations in the reactant species N_2 and O serve to increase the net forward reaction rate, particularly near the peak-temperature location, joint fluctuations in the product species correspondingly increase the backwards component of the reaction, apart from the region between the peak-temperature location and $y^* \simeq 200$, where the anticorrelation in the product partial densities serves to effectively increase the significance of the forward reaction rate. For the second of the Zel'dovich reactions, joint partial-density fluctuations in O_2 and N account almost entirely for the distortion in the mean reaction rate associated with $\overline{\mathcal{I}}^{\rho_j}_{\mathcal{R}_i}$, significantly increasing the effective forward reaction rate in the buffer and logarithmic layers, associated with anticorrelation between the product-species partial-density fluctuations.

The species-specific terms arising from the further decomposition of $\overline{\mathcal{I}}^{\rho_j,\theta}_{\mathcal{W}_i}$ can be directly evaluated as

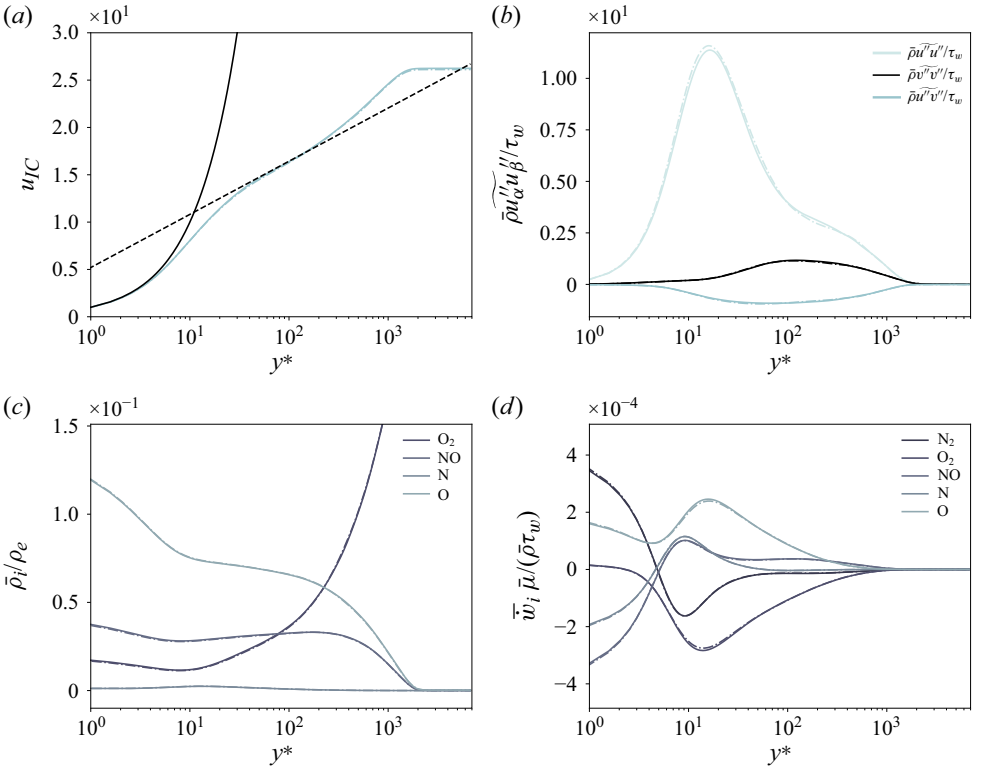

Figure 21. Mean wall-normal profiles of (*a*) transformed streamwise velocity, (*b*) normal Reynolds-stress components, (*c*) species partial densities and (*d*) chemical production rates. Solid lines correspond to the fine-grid numerical solution included in § 2, whereas the dash-dotted lines denote the coarse-grid results.

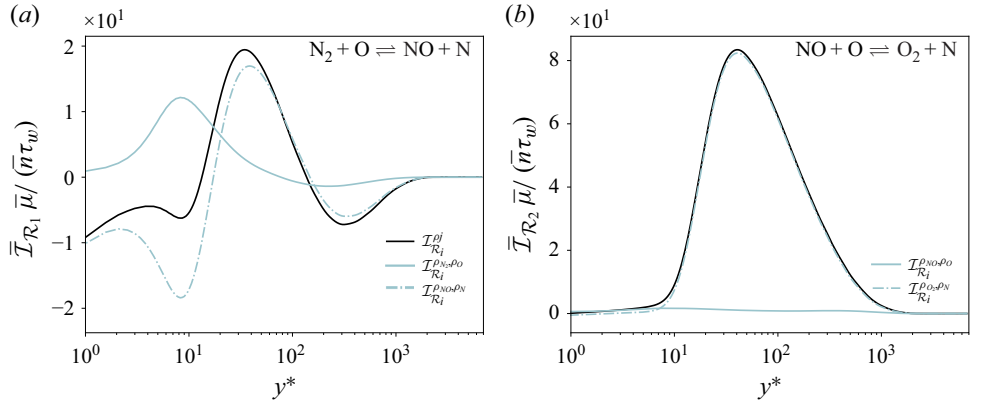

Figure 22. Fine-grained decomposition of turbulence–chemistry interaction induced by partial-density fluctuations for the Zel'dovich exchange reactions (*a*) (R1) and (*b*) (R2).

$$\overline{\mathcal{I}}^{\rho_\alpha,\theta}_{\mathcal{R}_i} = \int_{\mathbb{R}^{N_s+1}} \mathrm{d}\mathcal{V}\, \mathcal{R}_i(\{\rho_j\}, T)\mathcal{P}(\rho_\alpha, T) \prod_{\substack{\kappa=1,\\ \kappa\neq\alpha}}^{N_s} \delta(\rho_\kappa - \overline{\rho}_\kappa) - \overline{\mathcal{I}}^{\rho_\alpha}_{\mathcal{R}_i} - \overline{\mathcal{I}}^{\theta}_{\mathcal{R}_i} - \mathcal{R}_i^{mf}, \quad \text{(D5)}$$

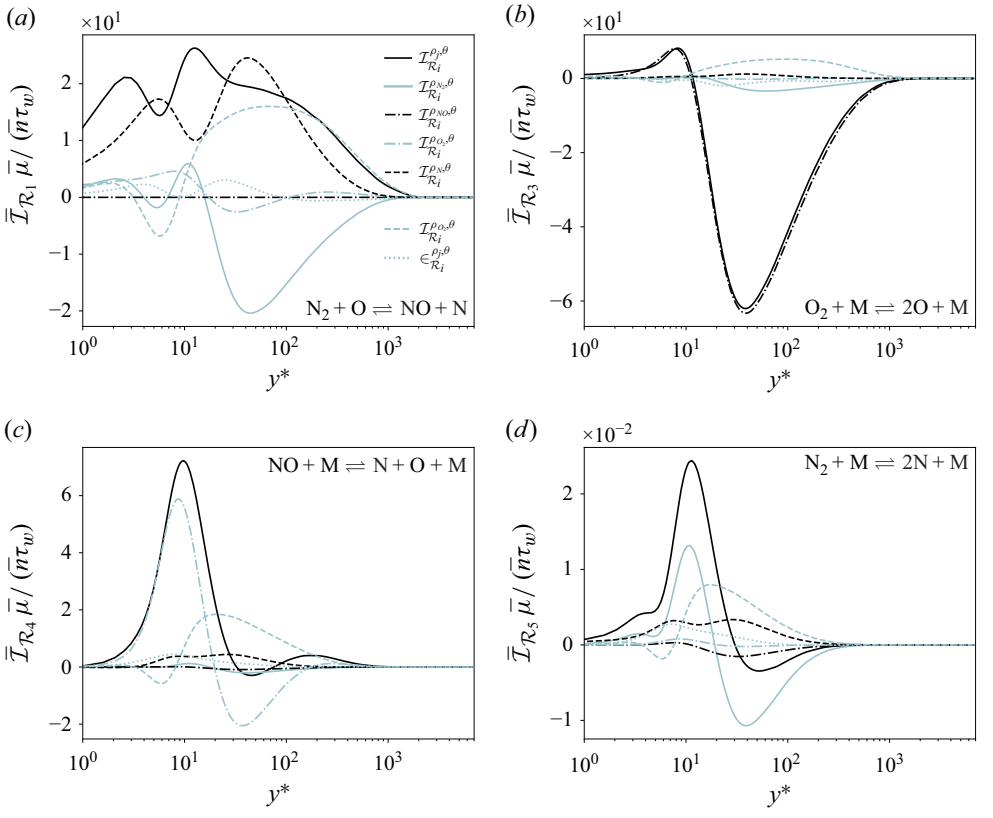

Figure 23. Fine-grained decomposition of turbulence–chemistry interaction arising jointly from temperature and partial-density fluctuations for the (*a*) first Zel'dovich reaction, R_1, as well as the dissociation/recombination of (*b*) molecular oxygen, (*c*) nitric oxide and (*d*) molecular nitrogen.

$$\overline{\epsilon}^{\rho_j,\theta}_{\mathcal{R}_i} = \overline{\mathcal{I}}^{\rho_j,\theta}_{\mathcal{W}_i} - \sum_{\alpha=1}^{N_s} \overline{\mathcal{I}}^{\rho_\alpha,\theta}_{\mathcal{R}_i}. \tag{D6}$$

For the first Zel'dovich reaction, joint fluctuations in temperature and both the reactant and product partial densities are shown to modulate the net reaction rate in figure 23. Whereas joint fluctuations in temperature and the atomic species' partial densities serve to increase the net forward reaction rate, the coupling between thermal and ρ_{N_2} fluctuations correspondingly serve to decrease the forward bias in the reaction rate. Overall, however, it is the joint fluctuations in temperature with ρ_O and ρ_N that ultimately prove more consequential, uniformly increasing the net forward bias of the reaction throughout the boundary layer. For the molecular-oxygen dissociation/recombination reaction, however, joint ρ_{O_2}/temperature fluctuations account almost entirely for the overall reaction-rate distortion due to the coupling between partial-density and temperature fluctuations, effectively suppressing the net forward reaction rate. Finally, for the dissociation/recombination of molecular nitrogen and nitric oxide, joint fluctuations in temperature and their respective reactant molecules again prove the most consequential, manifesting in an increased net forward/dissociation reaction rate within the peak-temperature location. For these latter dissociation/recombination reactions, the coupling between temperature and radical-partial-density fluctuations

likewise contributes significantly to $\overline{\mathcal{I}}^{\rho_j,\theta}_{\mathcal{R}_i}$, particularly outside the peak-temperature location, where it effectively increases the forward bias of the respective reactions and largely balances the effect of joint fluctuations in temperature and the relevant reactant partial density.

References

Anderson, J.D.Jr. 2006 *Hypersonic and High-Temperature Gas Dynamics*, 2nd edn. American Institute of Aeronautics and Astronautics.

Bertin, J.J. & Cummings, R.M. 2006 Critical hypersonic aerothermodynamic phenomena. *Annu. Rev. Fluid Mech.* **38** (1), 129–157.

Bertolotti, F.P. 1998 The influence of rotational and vibrational energy relaxation on boundary-layer stability. *J. Fluid Mech.* **372**, 93–118.

Bird, R.B., Stewart, W.E. & Lightfoot, E.N. 1960 *Transport Phenomena*. John Wiley & Sons, Inc.

Bradshaw, P. 1977 Compressible turbulent shear layers. *Annu. Rev. Fluid Mech.* **9**, 33–52.

Candler, G.V. 2019 Rate effects in hypersonic flows. *Annu. Rev. Fluid Mech.* **51** (1), 379–402.

Capitelli, M., Armenise, I. & Gorse, C. 1997 State-to-state approach in the kinetics of air components under re-entry conditions. *J. Thermophys. Heat Transfer* **11** (4), 570–578.

Ceci, A., Palumbo, A., Larsson, J. & Pirozzoli, S. 2022 Numerical tripping of high-speed turbulent boundary layers. *Theor. Comput. Fluid Dyn.* **36** (6), 865–886.

Coffee, T.P. & Heimerl, J.M. 1981 Transport algorithms for premixed, laminar steady-state flames. *Combust. Flame* **43** (C), 273–289.

Cogo, M., Baù, U., Chinappi, M., Bernardini, M. & Picano, F. 2023*a* Assessment of heat transfer and Mach number effects on high-speed turbulent boundary layers. *J. Fluid Mech.* **974**, A10.

Cogo, M., Salvadore, F., Picano, F. & Bernardini, M. 2022 Direct numerical simulation of supersonic and hypersonic turbulent boundary layers at moderate-high Reynolds numbers and isothermal wall condition. *J. Fluid Mech.* **945**, A30.

Cogo, M., Williams, C.T., Griffin, K.P., Picano, F. & Moin, P. 2023*b* *Inverse-Velocity Transformation Wall Model for Reacting Turbulent Hypersonic Boundary Layers*, pp. 203–216. Annual Research Briefs, Center for Turbulence Research, Stanford University.

Curtiss, C.F. & Hirschfelder, J.O. 1949 Transport properties of multicomponent gas mixtures. *J. Chem. Phys.* **17** (6), 550–555.

Di Renzo, M., Fu, L. & Urzay, J. 2020 HTR solver: an open-source exascale-oriented task-based multi-GPU high-order code for hypersonic aerothermodynamics. *Comput. Phys. Commun.* **255**, 107262.

Di Renzo, M. & Urzay, J. 2021 Direct numerical simulation of a hypersonic transitional boundary layer at suborbital enthalpies. *J. Fluid Mech.* **912**, A29.

Di Renzo, M., Williams, C.T. & Pirozzoli, S. 2024 Stagnation enthalpy effects on hypersonic turbulent compression corner flow at moderate Reynolds numbers. *Phys. Rev. Fluids* **9**, 033401.

Donzis, D.A. & Jagannathan, S. 2013 Fluctuations of thermodynamic variables in stationary compressible turbulence. *J. Fluid Mech.* **733**, 221–244.

van Driest, E. 1956 The problem of aerodynamic heating. *Aeronaut. Engng Rev.* **15**, 26–41.

Duan, L., Beekman, I. & Martin, M.P. 2010 Direct numerical simulation of hypersonic turbulent boundary layers. Part 2. Effect of wall temperature. *J. Fluid Mech.* **655**, 419–445.

Duan, L., Beekman, I. & Martin, M.P. 2011 Direct numerical simulation of hypersonic turbulent boundary layers. Part 3. Effect of Mach number. *J. Fluid Mech.* **672**, 245–267.

Duan, L. & Martin, M.P. 2009 Effect of finite-rate chemical reactions on turbulence in hypersonic turbulence boundary layers. In *47th AIAA Aerospace Sciences Meeting Including the New Horizons Forum and Aerospace Exposition*. AIAA Paper 2009-0588.

Duan, L. & Martín, M.P. 2011 Assessment of turbulence-chemistry interaction in hypersonic turbulent boundary layers. *AIAA J.* **49** (1), 172–184.

Ern, A. & Giovangigli, V. 1994 Multicomponent Transport Algorithms. Lecture Notes in Physics Monographs m24. Springer.

Fan, Y., Li, W. & Pirozzoli, S. 2022 Energy exchanges in hypersonic flows. *Phys. Rev. Fluids* **7**, L092601.

Franko, K.J. & Lele, S.K. 2013 Breakdown mechanisms and heat transfer overshoot in hypersonic zero pressure gradient boundary layers. *J. Fluid Mech.* **730**, 491–532.

Fu, L., Hu, X.Y. & Adams, N.A. 2016 A family of high-order targeted ENO schemes for compressible-fluid simulations. *J. Comput. Phys.* **305**, 333–359.

Fujii, K. & Hornung, H.G. 2003 Experimental investigation of high-enthalpy effects on attachment-line boundary-layer transition. *AIAA J.* **41** (7), 1282–1291.

GERMAIN, P.D. & HORNUNG, H.G. 1997 Transition on a slender cone in hypervelocity flow. *Exp. Fluids* **22** (3), 183–190.

GIBIS, T., SCIACOVELLI, L., KLOKER, M. & WENZEL, C. 2024 Heat-transfer effects in compressible turbulent boundary layers – a regime diagram. *J. Fluid Mech.* **995**, A14.

GNOFFO, P.A., GUPTA, R.N. & SHINN, J.L. 1989 Conservation equations and physical models for hypersonic air flows in thermal and chemical nonequilibrium. *NASA technical paper* 2867. National Aeronautics and Space Administration, Office of Management, Scientific and Technical Information Division.

GOTTLIEB, S., SHU, C.-W. & TADMOR, E. 2001 Strong stability-preserving high-order time discretization methods. *SIAM Rev.* **43** (1), 89–112.

GRIFFIN, K.P., FU, L. & MOIN, P. 2021 Velocity transformation for compressible wall-bounded turbulent flows with and without heat transfer. *Proc. Natl Acad. Sci.* **118** (34), e2111144118.

GRIFFOND, J. 2005 Linear interaction analysis applied to a mixture of two perfect gases. *Phys. Fluids* **17** (8), 086101.

GUARINI, S.E., MOSER, R.D., SHARIFF, K. & WRAY, A. 2000 Direct numerical simulation of a supersonic turbulent boundary layer at Mach 2.5. *J. Fluid Mech.* **414**, 1–33.

HASAN, A.M., COSTA, P., LARSSON, J., PIROZZOLI, S. & PECNIK, R. 2024 Intrinsic compressibility effects in near-wall turbulence. arXiv: 2406.07649

HASAN, A.M., LARSSON, J., PIROZZOLI, S. & PECNIK, R. 2023 Incorporating intrinsic compressibility effects in velocity transformations for wall-bounded turbulent flows. *Phys. Rev. Fluids* **8**, L112601.

HUANG, J., DUAN, L. & CHOUDHARI, M.M. 2022 Direct numerical simulation of hypersonic turbulent boundary layers: effect of spatial evolution and Reynolds number. *J. Fluid Mech.* **937**, A3.

HUANG, P.G., COLEMAN, G.N. & BRADSHAW, P. 1995 Compressible turbulent channel flows: DNS results and modelling. *J. Fluid Mech.* **305**, 185–218.

HUDSON, M.L., CHOKANI, N. & CANDLER, G.V. 1997 Linear stability of hypersonic flow in thermochemical nonequilibrium. *AIAA J.* **35** (6), 958–964.

HUNT, J.C.R., WRAY, A.A. & MOIN, P. 1988 Eddies, streams, and convergence zones in turbulent flows. Studying turbulence using numerical simulation databases, 2. In *Proceedings of the 1988 summer program*.

INGER, G.R. 1964 Highly nonequilibrium boundary-layer flows of a multicomponent dissociated gas mixture. *Intl J. Heat Mass Transfer* **7**, 1151–1174.

JOHNSON, H.B., SEIPP, T.G. & CANDLER, G.V. 1998 Numerical study of hypersonic reacting boundary layer transition on cones. *Phys. Fluids* **10** (10), 2676–2685.

KLINE, H.L., CHANG, C.-L. & LI, F. 2018 Hypersonic chemically reacting boundary-layer stability using lastrac. In *2018 Fluid Dynamics Conference*. *AIAA Paper* 2018-3699.

KNISELY, C.P. & ZHONG, X. 2019 *Impact of Thermochemical Nonequilibrium Effects On the Supersonic Mode in Hypersonic Boundary Layers*. AIAA SciTech Forum.

KOVASZNAY, L.S.G. 1953 Turbulence in supersonic flow. *J. Aeronaut. Sci.* **20** (10), 657–674.

LANDAU, L.V. & TELLER, E. 1936 Zur theorie der schalldispersion. *Phys. Z. Sow*. **10**, 34–43.

LEE, J.-H. 1984 Basic governing equations for the flight regimes of aeroassisted orbital transfer vehicles. In *Thermal Design of Aeroassisted Orbital Transfer Vehicles* (ed. H.F. Nelson), pp. 3–53. American Institute of Aeronautics and Astronautics.

LEES, L. 1956 Laminar heat transfer over blunt-nosed bodies at hypersonic flight speeds. *J. Jet Propul.* **26** (4), 259–269.

LELE, S.K. 1994 Compressibility effects on turbulence. *Annu. Rev. Fluid Mech.* **26** (1), 211–254.

LIÑÁN, A. & DA RIVA, I. 1962 Chemical nonequilibrium effects in hypersonic aerodynamics. *Tech. Rep.* DTIC Report AD0294638.

LIVESCU, D. 2020 Turbulence with large thermal and compositional density variations. *Annu. Rev. Fluid Mech.* **52** (1), 309–341.

LYTTLE, I. & REED, H. 2005 Sensitivity of second-mode linear stability to constitutive models within hypersonic flow. In *43rd AIAA Aerospace Sciences Meeting and Exhibit*, pp. 889. American Institute of Aeronautics and Astronautics.

MARTIN, M. & CANDLER, G. 2001 Temperature fluctuation scaling in reacting boundary layers. In *15th AIAA Computational Fluid Dynamics Conference*. *AIAA Paper* 2001-2717.

MARTIN, M.P. & CANDLER, G.V. 1998 Effect of chemical reactions on decaying isotropic turbulence. *Phys. Fluids* **10** (7), 1715–1724.

MARTIN, M.P. & CANDLER, G.V. 1999 Subgrid-scale model for the temperature fluctuations in reacting hypersonic turbulent flows. *Phys. Fluids* **11** (9), 2765–2771.

MARTIN, M.P. & CANDLER, G.V. 2000 DNS of a Mach 4 boundary layer with chemical reactions. *AIAA Paper* 2000-0399.

MARXEN, O., IACCARINO, G. & MAGIN, T.E. 2014 Direct numerical simulations of hypersonic boundary-layer transition with finite-rate chemistry. *J. Fluid Mech.* **755**, 35–49.
MATHUR, S., TONDON, P.K. & SAXENA, S.C. 1967 Thermal conductivity of binary, ternary and quaternary mixtures of rare gases. *Mol. Phys.* **12** (6), 569–579.
MCBRIDE, B.J., ZEHE, M.J. & GORDON, S. 2002 NASA glenn coefficients for calculating thermodynamic properties of individual species. *Tech. Rep*. NASA.
MCMULLEN, R.M., KRYGIER, M.C., TORCZYNSKI, J.R. & GALLIS, M.A. 2023 Molecular-gas-dynamics simulations of turbulent Couette flow over a mean-free-path-scale permeable substrate. *Phys. Rev. Fluids* **8**, 083401.
MILLIKAN, R.C. & WHITE, D.R. 1963 Systematics of vibrational relaxation. *J. Chem. Phys.* **39** (12), 3209–3213.
MIRÓ, M., FERNANDO, B., ETHAN, S., PINNA, F. & REED, H.L. 2019 High-enthalpy models for boundary-layer stability and transition. *Phys. Fluids* **31** (4), 044101.
MORKOVIN, M.V. 1962 Effects of compressibility on turbulent flows. *Mécanique De LA Turbulence* **367**, 380.
MORTENSEN, C.H. 2018 Toward an understanding of supersonic modes in boundary-layer transition for hypersonic flow over blunt cones. *J. Fluid Mech.* **846**, 789–814.
PANESI, M., MAGIN, T., BOURDON, A., BULTEL, A. & CHAZOT, O. 2009 Fire II flight experiment analysis by means of a collisional-radiative model. *J. Thermophys. Heat Transfer* **23** (2), 236–248.
PANESI, M., MUNAFÒ, A., MAGIN, T.E. & JAFFE, R.L. 2014 Nonequilibrium shock-heated nitrogen flows using a rovibrational state-to-state method. *Phys. Rev. E* **90**, 013009.
PARK, C. 1989 A review of reaction rates in high temperature air. *AIAA Paper* 1989-1740.
PARK, C. 1990 *Nonequilibrium Hypersonic Aerothermodynamics*. Wiley.
PARK, C. 1993 Review of chemical-kinetic problems of future NASA missions. I - Earth entries. *J. Thermophys. Heat Transfer* **7** (3), 385–398.
PASSIATORE, D., GLOERFELT, X., SCIACOVELLI, L., PASCAZIO, G. & CINNELLA, P. 2024 Direct numerical simulation of subharmonic second-mode breakdown in hypersonic boundary layers with finite-rate chemistry. *Intl J. Heat Fluid Flow* **109**, 109505.
PASSIATORE, D., SCIACOVELLI, L., CINNELLA, P. & PASCAZIO, G. 2022 Thermochemical non-equilibrium effects in turbulent hypersonic boundary layers. *J. Fluid Mech.* **941**, A21.
PATEL, A., BOERSMA, B.J. & PECNIK, R. 2016 The influence of near-wall density and viscosity gradients on turbulence in channel flows. *J. Fluid Mech.* **809**, 793–820.
PETERS, N. & WARNATZ, J. 2013 *Numerical Methods in Laminar Flame Propagation: A GAMM-Workshop*, vol. 6. Springer-Verlag.
PIROZZOLI, S. 2010 Generalized conservative approximations of split convective derivative operators. *J. Comput. Phys.* **229** (19), 7180–7190.
PIROZZOLI, S. & BERNARDINI, M. 2011 Turbulence in supersonic boundary layers at moderate Reynolds number. *J. Fluid Mech.* **688**, 120–168.
PIROZZOLI, S., GRASSO, F. & GATSKI, T.B. 2004 Direct numerical simulation and analysis of a spatially evolving supersonic turbulent boundary layer at $M = 2.25$. *Phys. Fluids* **16** (3), 530–545.
RISTORCELLI, J.R. & BLAISDELL, G.A. 1997 Consistent initial conditions for the DNS of compressible turbulence. *Phys. Fluids* **9** (1), 4–6.
SEROR, S., ZEITOUN, D.E., BRAZIER, J.-P. & SCHALL, E. 1997 Asymptotic defect boundary layer theory applied to thermochemical non-equilibrium hypersonic flows. *J. Fluid Mech.* **339**, 213–238.
SMITS, A.J. & DUSSAUGE, J.-P. 2006 *Turbulent Shear Layers in Supersonic Flow*. Springer Science & Business Media.
STUCKERT, G. & REED, H.L. 1994 Linear disturbances in hypersonic, chemically reacting shock layers. *AIAA J.* **32** (7), 1384–1393.
TRETTEL, A. & LARSSON, J. 2016 Mean velocity scaling for compressible wall turbulence with heat transfer. *Phys. Fluids* **28** (2), 026102.
URZAY, J. 2018 Supersonic combustion in air-breathing propulsion systems for hypersonic flight. *Annu. Rev. Fluid Mech.* **50**, 593–627.
URZAY, J. & DI RENZO, M. 2021 *Engineering Aspects of Hypersonic Turbulent Flows at Suborbital Enthalpies*. Annual Research Briefs, Center for Turbulence Research.
VALENTINI, P., GROVER, M.S. & BISEK, N.J. 2024 Validity of Stokes' hypothesis for near-continuum hypersonic flows. *Phys. Fluids* **36** (5), , 051702.
VINCENTI, W.G. & KRÜGER, C.H. 1965 *Introduction to Physical Gas Dynamics*. Wiley.
WILKE, C.R. 1950 A viscosity equation for gas mixtures. *J. Chem. Phys.* **18** (4), 517–519.

WILLIAMS, C., DI RENZO, M., MOIN, P. & URZAY, J. 2021 *Locally self-similar formulation for hypersonic laminar boundary layers in thermochemical nonequilibrium*. Center for Turbulence Research Annual Research Briefs.

WILLIAMS, C.T., DI RENZO, M. & MOIN, P. 2022 *Computational Framework for Direct Numerical Simulation of Shock- Turbulence Interaction in Thermochemical Nonequilibrium*. Annual Research Briefs, Center for Turbulence Research, Stanford University.

WILLIAMS, C.T., DI RENZO, M. & MOIN, P. 2023 *Direct Simulation of Turbulence-Chemistry Interaction in a Strongly Reacting Turbulent Hypersonic Boundary Layer*. Annual Research Briefs, Center for Turbulence Research, Stanford University.

YU, M., XU, C.-X. & PIROZZOLI, S. 2019 Genuine compressibility effects in wall-bounded turbulence. *Phys. Rev. Fluids* **4**, 123402.

YU, M., XU, C.-X. & PIROZZOLI, S. 2020 Compressibility effects on pressure fluctuation in compressible turbulent channel flows. *Phys. Rev. Fluids* **5**, 113401.

ZEL'DOVICH, YA B. & RAIZER, YU P. 2002 *Physics of Shock Waves and High-Temperature Hydrodynamic Phenomena*. Dover.

ZHANG, C., DUAN, L. & CHOUDHARI, M.M. 2018 Direct numerical simulation database for supersonic and hypersonic turbulent boundary layers. *AIAA J.* **56** (11), 4297–4311.

ZHANG, Y.-S., BI, W.-T., HUSSAIN, F., LI, X.-L. & SHE, Z.-S. 2012 Mach-number-invariant mean-velocity profile of compressible turbulent boundary layers. *Phys. Rev. Lett.* **109**, 054502.